RESEARCH ARTICLE

INTERNATIONAL RESEARCH JOURNAL OF MULTIDISCIPLINARY TECHNOVATION

Asian Research Association

DOI: 10.54392/irjmt25215

Computational study on the Structural and Spectroscopic Properties, Solvent Effects, Topological Insights, and Biological Activities of 2-[1-(2, 4-dichlorobenzyl)-1H-indazol-3-yl] Propan-2-ol as an Anticonvulsant Drug

J. Jenifer [a], A. Ram Kumar [b], S. Selvaraj [a, *]

[a] Department of Physics, Saveetha School of Engineering, Saveetha Institute of Medical and Technical Sciences (SIMATS), Chennai, 602105, Tamil Nadu, India.

[b] Department of Biotechnology, Saveetha School of Engineering, Saveetha Institute of Medical and Technical Sciences (SIMATS), Chennai, 602105, Tamil Nadu, India.

* Corresponding Author Email: sselvaphy@gmail.com

DOI: https://doi.org/10.54392/irjmt25215

Received: 16-12-2024; Revised: 11-03-2025; Accepted: 22-03-2025; Published: 30-03-2025

Abstract: In this study, computational methods were employed to investigate the structural, vibrational, chemical shift, topological, thermodynamical, and biological properties of 2-[1-(2,4-dichlorobenzyl)-1H-indazol-3-yl]propan-2-ol (DCBIP), along with solvent effects on its electronic spectra, frontier molecular orbitals (FMO), and molecular electrostatic potential (MEP) surfaces. Molecular geometry analysis identified seven bond types and nine bond angles. Vibrational analysis confirmed 108 fundamental modes associated with OH, CO, CH, CC, CN, NN, CCl, CH_2, and CH_3 functional groups. Chemical shift analysis validated the structural integrity of DCBIP, with deshielding effects observed for key carbons and protons due to electronegative interactions, hydrogen bonding, and inductive effects from chlorine substituents. The consistent FMO energy gap (4.9797–4.9879 eV) across solvents suggests minimal solvent influence, with greater stability in polar environments. Natural bond orbital (NBO) analysis identified the strongest stabilization from the lone pair (LP) of N_4 donating to the antibonding $\sigma^*(C_8\text{-}C_9)$ orbital (40.25 kJ/mol), enhancing delocalization in the indazole ring. Mulliken analysis revealed O_3 as the most electronegative site and C_9 as the most electropositive, while MEP maps confirmed nucleophilic regions over O_3 and electrophilic sites over aromatic hydrogens. The specific heat capacity of DCBIP (77.31 cal $mol^{-1}K^{-1}$) reflects its moderate thermal energy absorption, influenced by vibrational contributions from its complex structure. Topological analyses highlighted electron localization at hydrogen atoms (H_{32}, H_{37}), delocalization in six-membered rings, and the presence of van der Waals interactions and steric effects in DCBIP. Molecular docking studies of DCBIP with 1EOU and 5FDC demonstrated strong binding affinities of -6.89 kcal/mol and -7.45 kcal/mol, respectively, suggesting its potential as an anticonvulsant agent.

Keywords: DFT, Solvent Effect, NBO, Chemical Shifts, MEP, Molecular Docking

1. Introduction

Indazoles are nitrogen-containing heterocyclic structures, also referred to as benzpyrazole and isoindazole. Structurally, indazole consists of a benzene fused with a pyrazole moiety, with the chemical formula of $C_7H_6N_2$. It is naturally extracted from *Nigella* plants and exists in tautomeric forms as 1*H* -indazole and 2*H*-isoindazole tautomeric forms [1, 2]. In recent decades, nitrogen-containing heterocyclic compounds, particularly derivatives of indazoles, have gained significant attention in drug discovery and medicinal chemistry due to their diverse biological activities [3-5]. Indazole derivatives are widely utilized in the pharmaceutical industry for their anticancer, antiarrhythmic, antifungal, and antiviral properties [6-14]. Notably, between 2016 and 2020, the Food and Drug Administration (FDA) has approved more than 23 indazole-based drugs for cancer treatment [15]. For instance, pazopanib, an indazole derivative, acts as an antagonist against the tyrosine kinase enzyme involved in renal cell carcinoma [16]. Similarly, axitinib and entrectinib inhibit tyrosine kinase and tropomyosin receptor kinases, respectively [17, 18]. Among indazole derivatives, 2-[1-(2-4-dichlorobenzyl)-1H-indazol-3-yl]propan-2-ol (DCBIP) is a nitrogen-containing heteroaromatic compound with a molecular mass of 335.2 g/mol and the chemical formula of $C_{17}H_{16}Cl_2N_2O$. Structurally, DCBIP comprises a chlorinated benzyl

moiety fused with an indazole core, encompassing two hydrogen bond acceptors and one hydrogen bond donor.

Over the past few decades, Density Functional Theory (DFT) has emerged as a cost-effective and reliable approach for exploring the structural, physicochemical, and spectroscopic properties of both synthetic and naturally derived compounds compared to other quantum chemical methods [19]. Theoretical investigations on the tautomerism of indazole in solvent (aqueous) and gas phases using DFT and *ab initio* methods have been previously reported [20]. Additionally, the structural and spectroscopic properties of indazole derivatives, such as 1H-indazole-3-carbaldehyde, have been analyzed using DFT techniques [21]. Furthermore, an extensive spectroscopic analysis of pazopanib has been performed [22]. Beyond structural studies, indazole derivatives have also demonstrated promising biological activities. For instance, the *in-vivo* anticonvulsant activity of 7-nitroindazole has been shown to be dose-dependent in a maximal electroshock-induced seizure model. In addition, the anticonvulsant potential of various indazole derivatives has been previously reported [23, 24].

Despite the extensive research on indazole derivatives, a comprehensive literature review indicates that no prior studies have investigated the theoretical and spectroscopic properties of DCBIP. In view of these facts, the present study aims to provide a comprehensive theoretical investigation of the molecular structure of DCBIP, including an analysis of its structural and spectroscopic properties, solvent effects in both polar and non-polar environments, and biological characteristics to gain deeper insights into its molecular behavior.

2. Computational Methods

All computational calculations were carried out using the DFT/B3LYP/6-31G(d,p) method, as included in the Gaussian 09W program package [25-32]. The electronic properties and chemical shifts of carbon and hydrogen were simulated using the Time Dependent-Density Functional Theory (TD-DFT) [33-35] and Gauge-Including Atomic Orbital (GIAO) approach [36-40] both employing the same basis set, respectively. The results were visualized using GaussView 6 [41] and Chemcraft program (version 1.6) [42]. The SwissADME tool, a free online predictor developed by the Swiss Institute of Bioinformatics [43], was utilized to evaluate Absorption, Distribution, Metabolism, and Excretion (ADME) properties of DCBIP, with the Simplified Molecular-Input Line-Entry System (SMILES) representation. Molecular docking simulations were performed using AutoDock (version 1.5.7) [44] to assess the interaction between DCBIP and its target macromolecule. The resulting ligand-protein complexes were analyzed in 2D and 3D using LigPlot+ [45] and PyMOL [46], respectively. Topological analysis of DCBIP was conducted using Multiwfn (version 3.8) and the Atomistica. online web application [47-49].

3. Results and Discussion

3.1. Structural parameters

The optimized structure of DCBIP, along with the numbering of atoms, is illustrated in Fig. 1, and the corresponding bond parameters are summarized in Table 1. Since the crystal structure of DCBIP has not yet been experimentally determined, this study employs the structurally related lonidamine pyridine-4-carboxamide for experimental comparison [50]. The simulated molecular geometry of DCBIP consists of seventeen C-C, fifteen C-H, three C-N, two C-Cl, one C-O, N-N and O-H bond lengths. Additionally, the structure includes twenty C-C-C, twenty-two C-C-H, two N-C-H, seven H-C-H, five N-C-C, four C-Cl-Cl, three N-N-C, three O-C-C, and one of each C-O-H and C-N-C bond angles. In DCBIP, the C-C bond lengths were predicted to range from 1.386 to 1.517 Å, while experimentally observed values fall within 1.375 to 1.512 Å. Notably, the bond lengths of C_6-C_{11} and C_6-C_{12} were slightly elongated as compared with other carbon atoms, due to the influence of electronegative oxygen (O_3). The C-N and C-H bond lengths were simulated between 1.321-1.451 and 1.083-1.097 Å, whereas experimental values were reported between 1.332-1.461 Å and 0.949-0.990 Å, respectively. Furthermore, the N-N bond length was theoretically predicted at 1.364 Å and observed at 1.347 Å.

The bond angles involving carbon atoms (C-C-C) were calculated to range between 117.0° and 123.6°, while experimentally observed values varied from 116.73° to 129.60°. Notably, the bond angles of C_6-C_7-C_8 and C_{10}-C_{15}-C_{18} were simulated at 128.1° and 123.6°, which exceed the standard 120° by 8.1° and 3.6°, respectively, due to the electronic effects of chlorine and nitrogen atoms. The C_6-O_3-H_{34} and C_9-N_4-C_{10} bond angles were theoretically predicted at 106.5° and 128.6°, whereas the experimentally determined C_9-N_4-C_{10} angle was found to be 128.80°. Furthermore, the bond angles for N-C-H, N-N-C, and N-C-C were simulated to be within 106.3°–108.4°, 107.0°–119.4°, and 106.2°–131.4°, while corresponding observed values ranged from 109.05°–109.10°, 106.0°–118.8°, and 106.0°–131.18°, respectively. Additionally, the C-C-H, O-C-C, and H-C-H bond angles were calculated within 109.8°–121.7°, 106.6°–109.4°, and 107.7°–108.6°, with experimental values reported between 109.05°–121.67° for C-C-H. The simulated bond parameters show a strong correlation with literature-reported values, yielding linear correlation coefficients (R^2) of 0.99661 for bond lengths and 0.98054 for bond angles. The correlation graph illustrating bond distances and bond angles is presented in Figure. S1 (Supplementary Material).

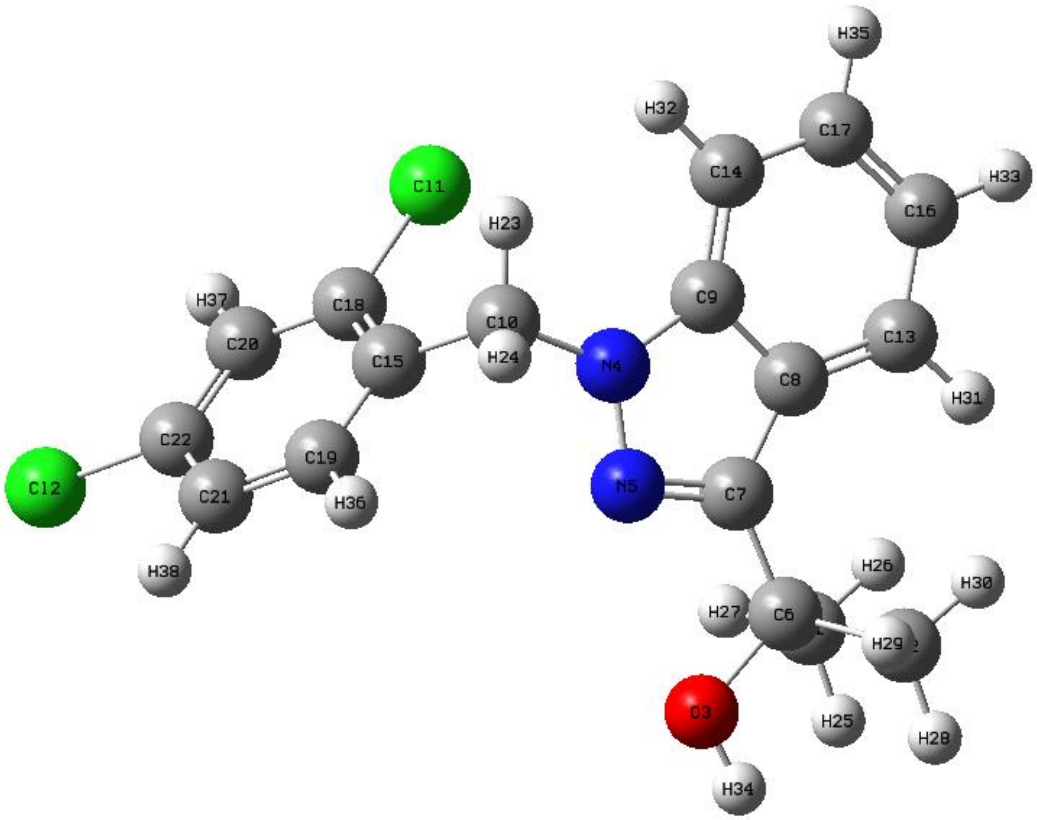

Figuer 1. Optimized molecular structure of DCBIP

Table 1. Geometrical parameters (bond lengths and bond angles) of DCBIP

Bond lengths (Å)	Theo.	* Exp.	Bond lengths (Å)	Theo.	* Exp.
Cl_1-C_{18}	1.767	1.734	C_{11}-H_{27}	1.093	-
Cl_2-C_{22}	1.756	1.743	C_{12}-H_{28}	1.097	-
O_3-C_6	1.429	-	C_{12}-H_{29}	1.093	-
O_3-H_{34}	0.967	-	C_{12}-H_{30}	1.094	-
N_4-N_5	1.364	1.347	C_{13}-C_{16}	1.386	1.375
N_4-C_9	1.370	1.374	C_{13}-H_{31}	1.085	0.949
N_4-C_{10}	1.451	1.461	C_{14}-C_{17}	1.386	1.376
N_5-C_7	1.321	1.332	C_{14}-H_{32}	1.085	0.950
C_6-C_7	1.517	1.479	C_{15}-C_{18}	1.400	1.390
C_6-C_{11}	1.541	-	C_{15}-C_{19}	1.403	1.396
C_6-C_{12}	1.541	-	C_{16}-C_{17}	1.414	1.413
C_7-C_8	1.439	1.424	C_{16}-H_{33}	1.086	0.950
C_8-C_9	1.418	1.407	C_{17}-H_{35}	1.086	0.950
C_8-C_{13}	1.409	1.409	C_{18}-C_{20}	1.396	1.387
C_9-C_{14}	1.405	1.404	C_{19}-C_{21}	1.391	1.384
C_{10}-C_{15}	1.521	1.512	C_{19}-H_{36}	1.086	0.949
C_{10}-H_{23}	1.090	0.990	C_{20}-C_{22}	1.391	1.380
C_{10}-H_{24}	1.093	0.989	C_{20}-H_{37}	1.083	0.950
C_{11}-H_{25}	1.097	-	C_{21}-C_{22}	1.395	1.385
C_{11}-H_{26}	1.093	-	C_{21}-H_{38}	1.084	0.949

Bond angles (◦)	Theo.	* Exp.	Bond angles (◦)	Theo.	* Exp.
Cl_1-C_{18}-C_{15}	121.10	120.78	C_8-C_{13}-H_{31}	121.10	121.00
Cl_1-C_{18}-C_{20}	116.80	116.70	C_9-C_{14}-C_{17}	117.00	116.73
Cl_2-C_{22}-C_{20}	119.10	117.83	C_9-C_{14}-H_{32}	121.70	121.59
Cl_2-C_{22}-C_{21}	119.70	120.35	C_{15}-C_{10}-H_{23}	110.80	109.05
C_6-O_3-H_{34}	106.50	-	C_{15}-C_{10}-H_{24}	109.80	109.06
O_3-C_6-C_7	106.60	-	C_{10}-C_{15}-C_{18}	123.60	122.59
O_3-C_6-C_{11}	109.10	-	C_{10}-C_{15}-C_{19}	119.20	120.26
O_3-C_6-C_{12}	109.40	-	H_{23}-C_{10}-H_{24}	107.70	107.82
N_5-N_4-C_9	111.70	112.1	H_{25}-C_{11}-H_{26}	107.70	-
N_5-N_4-C_{10}	119.40	118.8	H_{25}-C_{11}-H_{27}	108.50	-
N_4-N_5-C_7	107.00	106.00	H_{26}-C_{11}-H_{27}	108.50	-
C_9-N_4-C_{10}	128.60	128.80	H_{28}-C_{12}-H_{29}	108.60	-
N_4-C_9-C_8	106.20	106.20	H_{28}-C_{12}-H_{30}	107.80	-
N_4-C_9-C_{14}	131.40	131.18	H_{29}-C_{12}-H_{30}	108.50	-
N_4-C_{10}-C_{15}	113.60	112.62	C_{16}-C_{13}-H_{31}	120.10	121.03
N_4-C_{10}-H_{23}	108.40	109.10	C_{13}-C_{16}-C_{17}	121.10	121.74
N_4-C_{10}-H_{24}	106.30	109.05	C_{13}-C_{16}-H_{33}	119.70	119.15
N_5-C_7-C_6	121.30	118.70	C_{17}-C_{14}-H_{32}	121.30	121.67
N_5-C_7-C_8	110.60	111.45	C_{14}-C_{17}-C_{16}	121.60	121.52
C_7-C_6-C_{11}	110.30	-	C_{14}-C_{17}-H_{35}	119.30	119.20
C_7-C_6-C_{12}	110.10	-	C_{18}-C_{15}-C_{19}	117.20	117.13
C_6-C_7-C_8	128.10	129.60	C_{15}-C_{18}-C_{20}	122.20	122.50
C_{11}-C_6-C_{12}	111.20	-	C_{15}-C_{19}-C_{21}	122.00	121.94
C_6-C_{11}-H_{25}	109.90	-	C_{15}-C_{19}-H_{36}	118.20	119.06
C_6-C_{11}-H_{26}	112.30	-	C_{17}-C_{16}-H_{33}	119.20	119.10
C_6-C_{11}-H_{27}	109.80	-	C_{16}-C_{17}-H_{35}	119.20	119.27
C_6-C_{12}-H_{28}	110.10	-	C_{18}-C_{20}-C_{22}	118.60	118.07
C_6-C_{12}-H_{29}	109.70	-	C_{18}-C_{20}-H_{37}	120.50	120.98
C_6-C_{12}-H_{30}	112.10	-	C_{21}-C_{19}-H_{36}	119.80	118.98
C_7-C_8-C_9	104.40	104.11	C_{19}-C_{21}-C_{22}	120.90	118.53
C_7-C_8-C_{13}	136.60	136.36	C_{19}-C_{21}-H_{38}	120.90	120.69
C_9-C_8-C_{13}	119.00	119.49	C_{22}-C_{20}-H_{37}	120.90	120.94
C_8-C_9-C_{14}	122.50	122.51	C_{20}-C_{22}-C_{21}	121.10	121.80
C_8-C_{13}-C_{16}	118.80	117.96	C_{22}-C_{21}-H_{38}	120.30	120.77

* Taken from Ref [50]

3.2. Vibrational properties

The DCBIP molecule consists of 38 atoms, exhibiting 108 fundamental vibrational modes, as determined by the 3N-6 rule, with C_1 point group symmetry. The calculated infrared (IR) and Raman spectra are illustrated in Figure. 2, with vibrational assignments listed in Table 2. To enhance accuracy, the simulated wavenumbers were corrected using a scaling factor of 0.96.

The O–H stretching vibration is observed at 3655 cm^{-1}, with a moderate IR intensity of 8.65 and a strong Raman activity of 161.71, indicating significant polarizability changes. The in-plane bending vibrations appear in the 1236 –1124 cm^{-1} region, overlapping with CH and CH_3 bending modes.

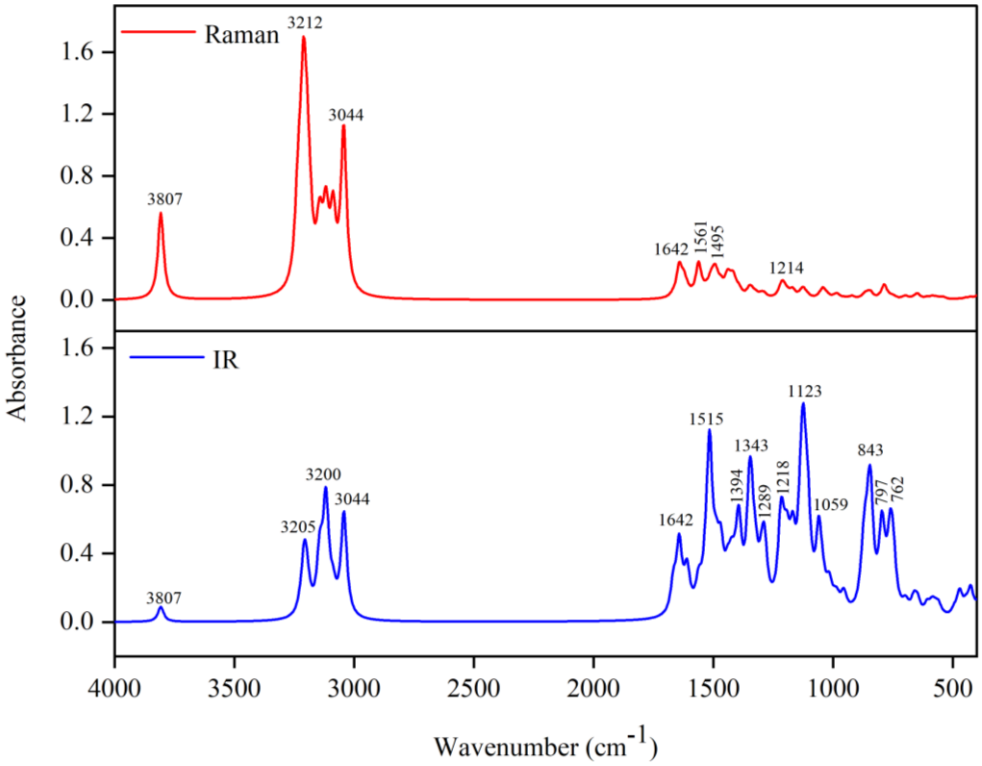

Figure 2. Simulated IR and Raman spectra of DCBIP

The out-of-plane bending vibrations typically occur in the lower wavenumber region 622 - 518 cm^{-1}. These assignments are further supported by previous reports [51]. The CH stretching vibrations occur in the 3108–3058 cm^{-1} range, with a prominent Raman activity of 288.54 at 3084 cm^{-1}, 98.80 at 3098 cm^{-1}, and 85.91 at 3108 cm^{-1}. The in-plane CH bending vibrations are observed between 1599–1001 cm^{-1}, with 1576 cm^{-1} displaying an IR intensity of 39.45 and 1499 cm^{-1} showing a Raman activity of 61.60. The out-of-plane CH bending vibrations occur in the 985–732 cm^{-1} range, with 732 and 818 cm^{-1} exhibiting the most prominent IR intensity of 37.42 and 22.97, respectively. These assignments align with findings from previous studies [52-54].

The asymmetric stretching vibrations of the methyl group appear around 3015, 2993 cm^{-1}, 2988 cm^{-1}, with the highest IR intensity of 58.32 at 2993 cm^{-1} and a peak Raman activity of 122.86, indicating strong polarizability changes. The symmetric stretching modes occur at 2922 cm^{-1}, and 2916 cm^{-1}, with 2922 cm^{-1} exhibiting a high IR intensity of 47.53 and a significant Raman activity of 286.37, reflecting structural sensitivity. Asymmetric bending vibrations are observed in the 1470–1435 cm^{-1} range, with a notable IR intensity of 80.29 at 1454 cm^{-1}. The symmetric bending modes, occurring between 1383–1367 cm^{-1}, show moderate IR and Raman responses. The literature provides additional evidence supporting these assignments [55]. For the methylene group, asymmetric stretching vibrations are observed at 3023 cm^{-1} and 3017 cm^{-1} with IR intensity of 21.60 and a Raman activity of 53.03. The symmetric stretching mode at 2964 cm^{-1} exhibits a moderate IR intensity of 11.79 but a strong Raman activity of 132.32, indicating significant vibrational contributions. Bending vibrations, including asymmetric and symmetric bending occurs below 1558 cm^{-1}, with a notable IR intensity and the highest Raman activity. The literature confirms the reliability of these vibrational assignments [56, 57].

The C–C stretching vibrations are observed in the 1599–1394 cm^{-1} range with the most intense IR peak appears at 1576 cm^{-1} with an IR intensity of 39.45 and a Raman activity of 55.86, indicating significant dipole moment and polarizability changes that aligns with an earlier report [58]. The C–N stretching vibrations appeared at 1353 and 1338 cm^{-1} (34.84 IR intensity), which are further supported by previous reports in the literature [59]. The prominent C–Cl stretching vibrations are observed at 1089, 1078, 1017, 765, and 718 cm^{-1}. Among these, 1078 cm^{-1} exhibits the highest IR intensity of 67.52, while 1089 cm^{-1} and 1017 cm^{-1} show significant IR intensities of 45.69 and 43.40, respectively. Raman activity is notable at 1078 cm^{-1} with a value of 14.09. The vibrational characteristics identified here align with previous findings [60]. In addition, the N-N and C-O stretching`s were calculated at 1271 and 1089 cm^{-1} have good correlation with literature findings [61, 62].

Table 2. Simulated vibrational assignments of DCBIP

Modes	Theoretical wavenumber (cm^{-1})				Vibrational assignments
	Unscaled	Scaled	IR Intensity	Raman activity	
1	3807	3655	8.65	161.71	υ OH
2	3238	3108	0.29	85.91	υ CH
3	3227	3098	1.35	96.80	υ CH
4	3212	3084	14.45	288.54	υ CH
5	3205	3077	23.20	28.81	υ CH
6	3200	3072	1.31	76.01	υ CH
7	3194	3066	11.04	104.11	υ CH
8	3185	3058	0.19	59.377	υ CH
9	3149	3023	2.03	30.33	υ_{as} CH_2
10	3143	3017	21.60	53.03	υ_{as} CH_2
11	3141	3015	9.67	31.47	υ_{as} CH_3
12	3118	2993	58.32	122.86	υ_{as} CH_3
13	3112	2988	6.81	11.99	υ_{as} CH_3
14	3088	2964	11.79	132.32	υ_{s} CH_2
15	3044	2922	47.53	286.37	υ_{s} CH_3
16	3038	2916	13.39	20.61	υ_{s} CH_3
17	1666	1599	16.65	3.55	β CH, υ CC
18	1642	1576	39.45	55.86	β CH, υ CC
19	1623	1558	0.40	26.29	β CH, υ CC, τ CH_2
20	1610	1546	23.31	7.91	β CH, υ CC, τ CH_2
21	1561	1499	14.42	61.60	β CH
22	1531	1470	14.61	7.05	δ_{as} CH_3, β CH
23	1518	1457	9.66	1.34	β CH, δ_{as} CH_3
24	1515	1454	80.29	1.87	χ CH_2, β CH, δ_{as} CH_3
25	1510	1450	1.69	21.24	δ_{as} CH_3
26	1497	1437	0.52	1.50	δ_{as} CH_3
27	1495	1435	0.01	25.87	δ_{as} CH_3
28	1488	1428	21.92	20.08	χ CH_2
29	1469	1410	29.84	17.05	χ CH_2, β CH
30	1441	1383	15.00	33.37	β CH, τ CH_2, δ_{s} CH_3, υ CC
31	1427	1370	3.31	6.84	δ_{s} CH_3
32	1424	1367	15.05	5.03	β CH, ω CH_2, δ_{s} CH_3
33	1416	1359	0.84	25.81	β CH, τ CH_2
34	1409	1353	8.40	1.90	υ CN

35	1394	1338	34.84	6.29	ω CH_2, β CH, υ CN, υ CC
36	1392	1336	10.68	6.36	β CH, ω CH_2
37	1350	1296	38.59	10.43	β CH
38	1343	1289	44.87	10.55	β CH, τ CH_2
39	1324	1271	19.41	7.31	υ NN, β CH, τ CH_2
40	1299	1247	14.36	5.76	β CH, τ CH_2
41	1287	1236	34.24	6.34	β CH, β OH, τ CH_2
42	1220	1171	7.10	5.95	β CH, β OH
43	1218	1169	35.39	6.47	β CH
44	1209	1161	13.12	20.10	β OH, τ CH_2, β CH
45	1194	1146	23.61	6.95	β OH
46	1186	1139	7.55	1.44	β CH, τ CH_2
47	1171	1124	3.86	3.52	β CH, β OH
48	1168	1121	28.30	10.94	β CH
49	1134	1089	45.69	6.59	β CH, τ CH_2, υ CCl, υ CO
50	1123	1078	67.52	14.09	β CH, υ CCl
51	1105	1061	45.37	3.68	β CH, τ CH_2
52	1059	1017	43.40	1.89	β CH, υ CCl
53	1043	1001	9.79	18.22	β CH
54	1026	985	0.06	4.54	γ CH
55	1016	975	14.12	0.98	γ CH, ρ CH_2
56	993	953	3.76	2.53	γ CH
57	983	944	5.79	7.03	γ CH
58	982	943	0.03	0.47	γ CH
59	955	917	10.32	1.58	ρ CH_2, γ CH
60	944	906	0.66	0.52	γ CH
61	922	885	0.04	4.96	γ CH
62	877	842	11.86	1.41	γ CH
63	867	832	27.55	4.31	γ CH, τ CH_2
64	863	828	0.36	2.81	γ CH
65	852	818	22.97	5.32	γ CH
66	843	809	55.14	8.94	γ CH, ω CH_2
67	797	765	40.65	0.85	ω CH_2, γ CH, υ CCl
68	789	757	1.91	1.55	γ CH
69	786	755	8.07	24.15	γ CH, τ CH_2
70	762	732	37.42	2.30	γ CH
71	748	718	26.96	3.93	ω CH_2, υ CCl
72	700	672	4.16	5.27	ω CH_2

73	693	665	2.66	0.70	ω CH_2
74	663	636	8.32	1.97	ω CH_2
75	648	622	8.35	9.57	γ OH, ω CH_2
76	607	583	6.02	3.19	γ OH, ρ CH_2
77	587	564	6.25	3.63	γ OH, δ NN
78	574	551	3.91	2.70	γ OH, ω CH_2
79	559	537	5.88	1.87	γ OH, ρ CH_2
80	540	518	0.80	3.91	γ OH, ρ CH_2
81	494	474	3.50	0.59	ω CH_2, γ CCl
82	472	453	13.764	0.98	τ CH_2
83	447	429	4.11	1.59	ρ CH_2, γ CH, δ CC
84	444	426	0.63	0.66	γ CH
85	426	409	15.14	3.44	γ CH, ω CH_2
86	399	383	1.54	2.39	ρ CH_2, γ CCl
87	396	380	3.49	2.83	ρ CH_2
88	388	372	2.22	2.93	ρ CH_2
89	345	331	0.92	1.85	ρ CH_2, δ CC
90	322	309	2.64	2.13	δ_{as} CH_3
91	306	294	0.74	0.59	δ_{as} CH_3, ρ CH_2
92	280	269	98.30	4.72	γ OH
93	275	264	1.91	1.40	ρ CH_2
94	264	253	3.66	0.69	δ_{as} CH_3
95	255	245	1.75	0.55	δ_{as} CH_3, ρ CH_2, γ CCl
96	245	235	0.66	0.57	δ_{as} CH_3
97	228	219	0.37	0.93	δ_{as} CH_2
98	208	200	0.81	1.93	δ_{as} CH_3
99	175	168	0.59	1.67	δ_{as} CH_3
100	173	166	0.03	1.64	δ_{as} CH_3, γ CCl
101	151	145	0.49	2.42	δ_{as} CH_3
102	128	123	1.54	1.12	γ OH, ρ CH_2, δ_{as} CH_3
103	107	103	1.00	4.93	γ OH, δ_{as} CH_3
104	88	84	0.75	1.23	ω CH_2, δ_{as} CH_3
105	48	46	0.94	1.28	γ OH, δ_{as} CH_3
106	28	27	0.35	3.58	δ Ring
107	23	22	0.62	5.50	δ Ring
108	14	13	0.19	4.62	δ Ring

υ_s - symmetric stretching; υ_{as} - asymmetric stretching; δ - bending / deformation; β – in-plane bending; γ – out-of-plane bending; χ - scissoring; ω - wagging; τ - twist; ρ – rocking, Scaling factor 0.96 for all vibrations.

3.3. Chemical shifts

The proton and carbon chemical shifts for DCBIP were simulated and presented in Table 3, and a comparison was made with ChemDraw predictions [63]. The C_6 carbon, central to the propanol side chain, exhibits a chemical shift of 62.843 ppm, indicating deshielding due to its attachment to the electronegative hydroxyl oxygen (O_3) and connectivity to two methyl groups (C_{11}, C_{12}). The hydroxyl proton exhibits significant shielding, indicating the presence of strong hydrogen bonding or intramolecular interactions with nearby functional groups. The C_7 carbon (135.284 ppm), part of the indazole system, bridges C_8 in the fused system and C_6 in the side chain. The adjacent C_8 (109.341 ppm) and C_9 (125.582 ppm) belong to the fused indazole ring, where C_9 is directly bonded to nitrogen (N4), leading to stronger deshielding compared to C_8. The C_{10} methylene carbon, which bridges the dichlorobenzyl ring and the indazole system, resonates at 39.286 ppm, reflecting partial deshielding due to its proximity to electronegative nitrogen (N_4) and chlorine atoms. The associated methylene protons H_{23} and H_{24}, with shifts at 5.649 ppm and 5.428 ppm, exhibit moderate deshielding due to interactions with adjacent aromatic and heteroaromatic systems. The methyl carbons (C_{11} and C_{12}) in the propan-2-ol side chain appear at 23.308 ppm and 23.339 ppm, indicating a relatively electron-rich environment. However, their corresponding protons (H_{25}, H_{26}, H_{27} and H_{28}, H_{29}, H_{30}) display chemical shifts ranging from 1.356 to 2.205 ppm. The indazole system exhibits aromatic proton shifts indicative of moderate deshielding effects. H_{31}, H_{32}, H_{33}, and H_{35} resonate between 7.276 and 7.826 ppm, reflecting the influence of the fused heterocyclic environment. Meanwhile, the corresponding carbons (C_{13}, C_{14}, C_{16}, and C_{17}) display chemical shifts ranging from 95.027 to 111.514 ppm, consistent with the expected electronic effects of the indazole ring system. The dichlorobenzyl ring carbons (C_{15}, C_{18}, C_{19}, C_{20}, C_{21}, and C_{22}) exhibit chemical shifts between 113.221 and 128.933 ppm, strongly influenced by the inductive effects of chlorine substituents. Notably, C_{18} (127.383 ppm) and C_{22} (128.933 ppm), which are directly bonded to chlorine atoms, show higher chemical shifts, confirming the strong electron-withdrawing effects of chlorine. The corresponding aromatic protons (H_{36}, H_{37}, H_{38}) within this system display chemical shifts ranging from 7.159 to 8.265 ppm, with H_{36} (8.265 ppm) showing the most downfield shift. These assignments align with previous reports [64] and ChemDraw predictions, reinforcing the structural integrity of the molecule and the reliability of chemical shift calculations.

3.4. Electronic characteristics

The electronic spectra of DCBIP in polar (acetone, methanol, and water) and non-polar (chloroform, cyclohexane, and toluene) solvents were simulated, as shown in Figure. 3. Additionally, the calculated wavelengths, excitation energies, and oscillator strengths are presented in Table 4.

Table 3. Simulated chemical shift values of DCBIP

Carbons	Chemical shifts (ppm)		Protons	Chemical shifts (ppm)	
	DFT	ChemDraw		DFT	ChemDraw
C_6	62.843	76.3	H_{23}	5.649	5.48
C_7	135.284	149.6	H_{24}	5.428	5.48
C_8	109.341	122.5	H_{25}	1.356	1.30
C_9	125.582	142.2	H_{26}	2.205	1.30
C_{10}	39.286	55.8	H_{27}	1.710	1.30
C_{11}	23.308	31.7	H_{28}	1.367	1.30
C_{12}	23.339	31.7	H_{29}	1.759	1.30
C_{13}	106.524	120.3	H_{30}	2.163	1.30
C_{14}	95.027	109.9	H_{31}	7.826	7.92
C_{15}	121.666	136.2	H_{32}	7.623	8.32
C_{16}	105.924	120.7	H_{33}	7.276	7.48
C_{17}	111.514	126.4	H_{34}	0.258	3.65
C_{18}	127.383	135.7	H_{35}	7.451	7.62
C_{19}	117.573	131.8	H_{36}	8.265	7.11
C_{20}	114.473	130.3	H_{37}	7.288	7.68
C_{21}	113.221	126.8	H_{38}	7.159	7.25
C_{22}	128.933	132.7	-	-	-

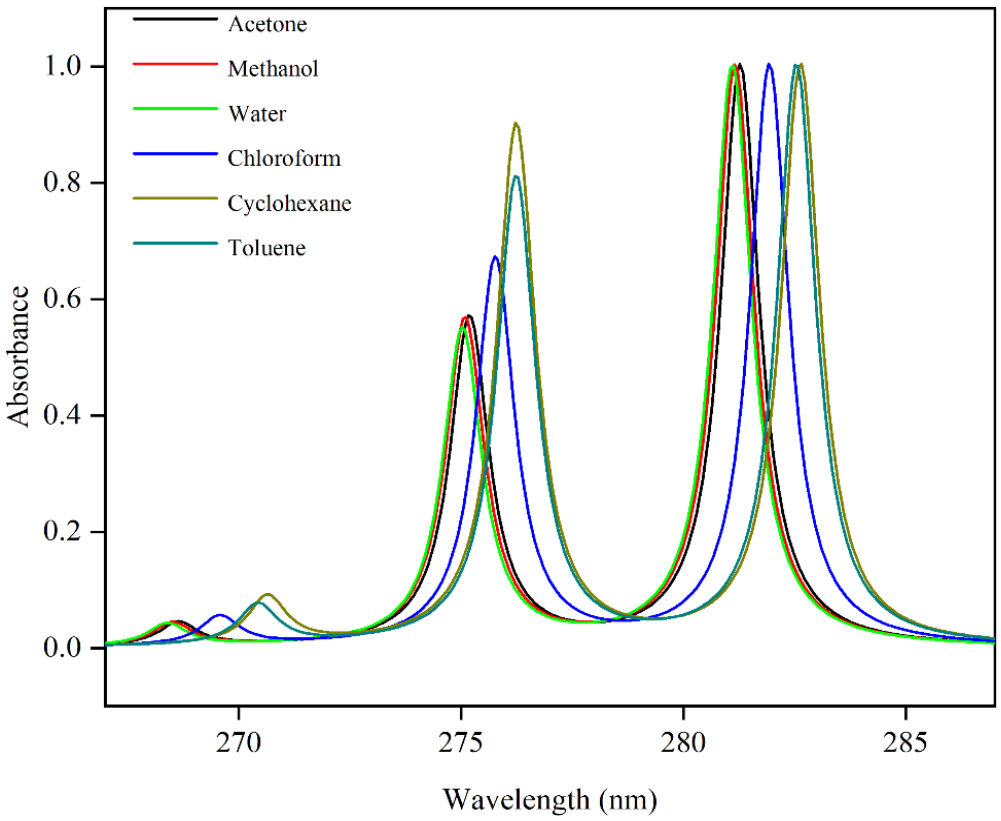

Figure 3. Theoretical electronic spectra of DCBIP in polar and nonpolar solvents

The frontier molecular orbitals (FMO) plots and density of states (DOS) spectra of DCBIP are depicted in Figs. 4 and 5, respectively, with the corresponding data provided in Table 5. In polar solvents, the most prominent absorption bands occur within the range of 281.10–281.27 nm, primarily arising from the HOMO → LUMO transition, which contributes 84–86% to the overall absorption. The corresponding excitation energies span from 4.4079 eV in acetone to 4.4106 eV in water, indicating a minimal variation in energy between solvents. The oscillator strengths, ranging from 0.1024 to 0.1041, suggest that this transition is highly allowed, with a significant probability of excitation. In non-polar solvents, a noticeable red shift is observed, with the absorption maxima shifting to the range of 281.93–282.63 nm. This shift is also attributed to the HOMO → LUMO transition (85–86% contribution), results from reduced solute-solvent interactions in non-polar environments, leading to a slight stabilization of the excited state. The oscillator strengths in this case are slightly lower (ranging from 0.0847 to 0.0993), which implies a marginally weaker transition probability compared to polar solvents. The excitation energies in non-polar solvents range from 4.3868 eV in cyclohexane to 4.3977 eV in chloroform, suggesting a slight stabilization of the excited state due to the non-polar environment.

In addition to the primary absorption band, a secondary band is observed in polar solvents at 275.03–275.19 nm, attributed to the HOMO → LUMO+1 transition (supporting a lower energy gap due to solvent effects.), with excitation energies ranging from 4.5053 eV in acetone to 4.5080 eV in water. The oscillator strengths (0.0567–0.0585) indicate a moderately allowed transition, A similar HOMO → LUMO+1 transition is also detected in non-polar solvents, occurring at slightly higher wavelengths (275.77–276.24 nm) with a similar contribution (86–87%). The oscillator strengths (0.0662 - 0.0759) indicate a moderately allowed transition, though with a reduced transition probability compared to the primary HOMO → LUMO transition. The excitation energies in non-polar solvents vary from 4.4882 eV (cyclohexane/toluene) to 4.4959 eV (chloroform).

A weaker absorption band is observed at 268.40–268.65 nm in polar solvents, corresponding to the HOMO → LUMO+2 transition, which contributes 97%. The oscillator strengths (~0.0040–0.0042), indicate that this transition is weakly allowed, with excitation energies ranging from 4.6150 eV to 4.6193 eV. Despite its dominant contribution, is less efficient due to the low oscillator strength. In non-polar solvents, the HOMO → LUMO+2 transition appears at slightly higher wavelengths (269.58–270.65 nm), with a similar dominant contribution of 96–97%. The oscillator strengths remain low (~0.0050–0.0070), further confirming the weakly allowed nature of this transition, with excitation energies ranging from 4.5810 eV to 4.5991 eV, slightly lower than in polar solvents, but still within a comparable energy range.

Table 4. Calculated wavelengths (λ), excitation energies (E), oscillator strength (f) of DCBIP

Solvents	λ (nm)	E (eV)	f	Major contributions	Minor contributions
Polar					
Water	281.10	0.1041	4.4106	H →L (84%)	H →L+1 (12%)
	275.03	0.0567	4.5080	H →L+1 (85%)	H →L (10%)
	268.40	0.0040	4.6193	H →L+2 (97%)	-
Methanol	281.16	0.1024	4.4098	H →L (86%)	H →L+1 (12%)
	275.09	0.0576	4.5071	H →L+1 (85%)	H →L (10%)
	268.52	0.0041	4.6173	H →L+2 (97%)	-
Acetone	281.27	0.1035	4.4079	H →L (84%)	H →L+1 (12%)
	275.19	0.0585	4.5053	H →L+1 (84%)	H →L (10%)
	268.65	0.0042	4.6150	H →L+2 (97%)	-
Non-polar					
Chloroform	281.93	0.0993	4.3977	H →L (85%)	H →L+1 (11%)
	275.77	0.0662	4.4959	H →L+1 (86%)	H →L (9%)
	269.58	0.0050	4.5991	H →L+2 (97%)	-
Cyclohexane	282.63	0.0847	4.3868	H →L (86%)	H →L+1 (11%)
	276.24	0.0759	4.4882	H →L+1 (86%)	H →L (8%)
	270.65	0.0070	4.5810	H →L+2 (96%)	-
Toluene	282.54	0.0919	4.3882	H →L (86%)	H →L+1 (10%)
	276.24	0.0741	4.4882	H →L+1 (87%)	H →L (8%)
	270.44	0.0064	4.5845	H →L+2 (97%)	-

Table 5. The FMO energies and energy gaps of DCBIP

Parameters	Formula	Acetone	Chloroform	Cyclohexane	Methanol	Toluene	Water
E_{HOMO} (eV)	-	-5.9021	-5.8640	-5.8286	-5.9075	-5.8368	-5.9130
E_{LUMO} (eV)	-	-0.9143	-0.8789	-0.8489	-0.9197	-0.8544	-0.9251
Energy gap (eV)	-	4.9878	4.9851	4.9797	4.9878	4.9824	4.9879
Ionization Potential (I) (eV)	$-E_{HOMO}$	5.9021	5.8640	5.8286	5.9075	5.8368	5.9130
Electron affinity (A) (eV)	$-E_{LUMO}$	0.9143	0.8789	0.8489	0.9197	0.8544	0.9251
Electronegativity (χ) (eV)	(I+A)/2	3.4082	3.3714	3.3387	3.4136	3.3456	3.4190
Chemical Potential (μ) (eV)	-χ	-3.4082	-3.3714	-3.3387	-3.4136	-3.3456	-3.4190
Chemical hardness (η) (eV)	(I-A)/2	2.4939	2.4925	2.4898	2.4939	2.4912	2.4939
Chemical softness (s) (eV^{-1})	1/2η	0.2004	0.2005	0.2008	0.2004	0.2007	0.2004
Global Electrophilicity (ω) (eV)	$\mu^2/2\eta$	2.3288	2.2801	2.2385	2.3362	2.2465	2.3436
Maximum electron charge (ΔNmax)	−(μ/η)	1.3666	1.3526	1.3409	1.3687	1.3429	1.3709

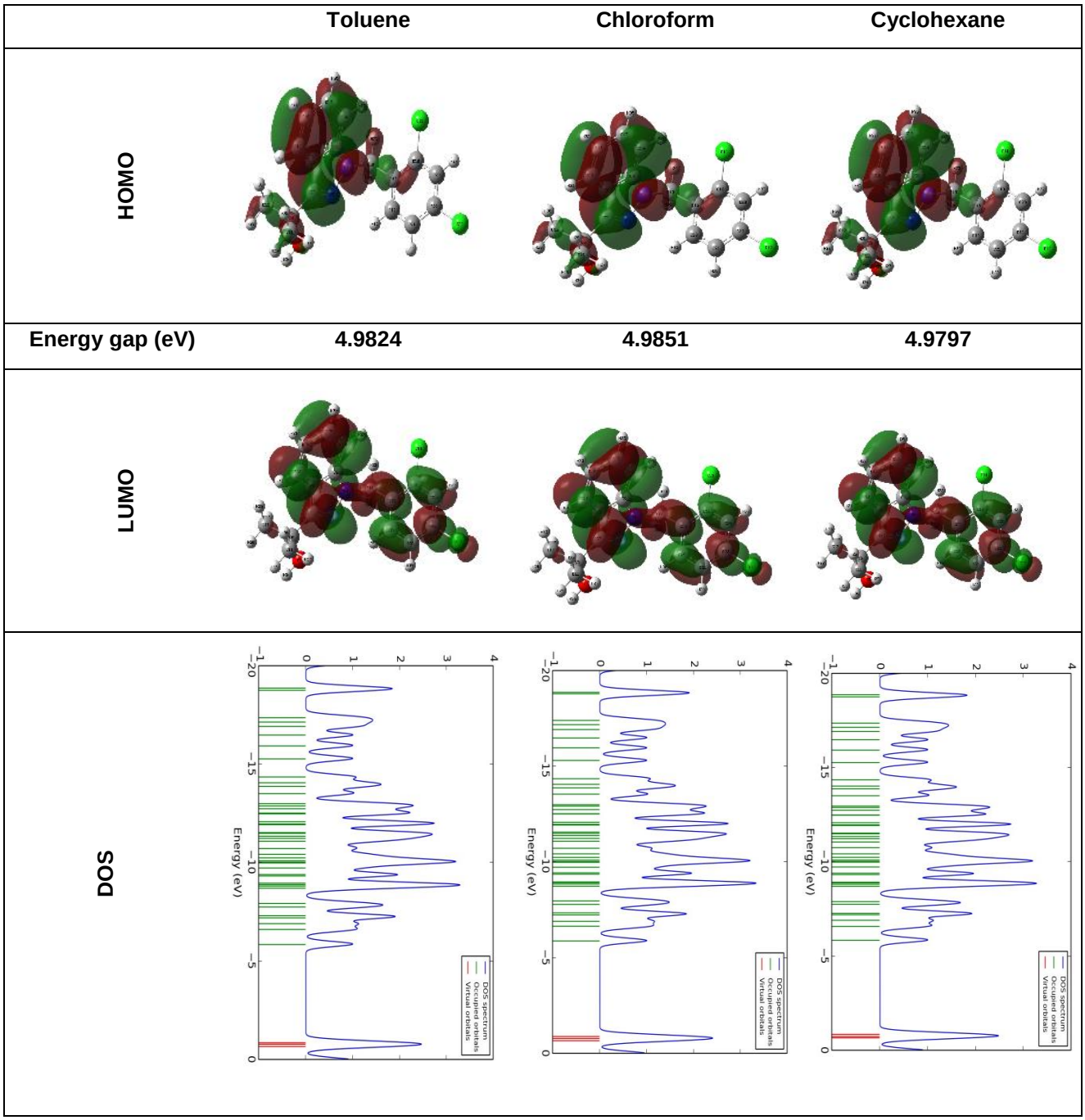

Figure 4. FMO plots and DOS spectra of DCBIP in the non-polar solvents

The FMO energy gap of DCBIP remains nearly consistent across solvents, ranging from 4.9797 eV in cyclohexane to 4.9879 eV in water, indicating minimal solvent influence on electronic excitation and stability. Since a higher energy gap correlates with greater stability, DCBIP is most stable in water (4.9879 eV) and methanol (4.9878 eV), while it is least stable in cyclohexane (4.9797 eV). Further supporting this, DCBIP is more stable in polar solvents due to its higher ionization potential, which is highest in water (5.9130 eV) and methanol (5.9075 eV), and lowest in cyclohexane (5.8286 eV). The greater HOMO stabilization in polar media reduces electron loss, lowering oxidation susceptibility. Similarly, the electron affinity follows a similar trend, with higher values in polar solvents (0.9251 eV in water) and methanol (0.9197 eV), while lower values in non-polar solvents (0.8489 eV in cyclohexane), enhancing its electron-accepting ability and stability in these environments. The increased electronegativity and chemical potential in polar solvents indicate stronger electron-withdrawing behavior, favoring charge stabilization. The electrophilicity index follows the same trend, with the highest value in water (2.3436 eV), indicating that DCBIP is better stabilized in polar solvents due to enhanced charge accommodation. Additionally, the maximum electron charge transfer is highest in polar solvents (1.3709 in water), supporting enhanced charge accommodation and molecular stability.

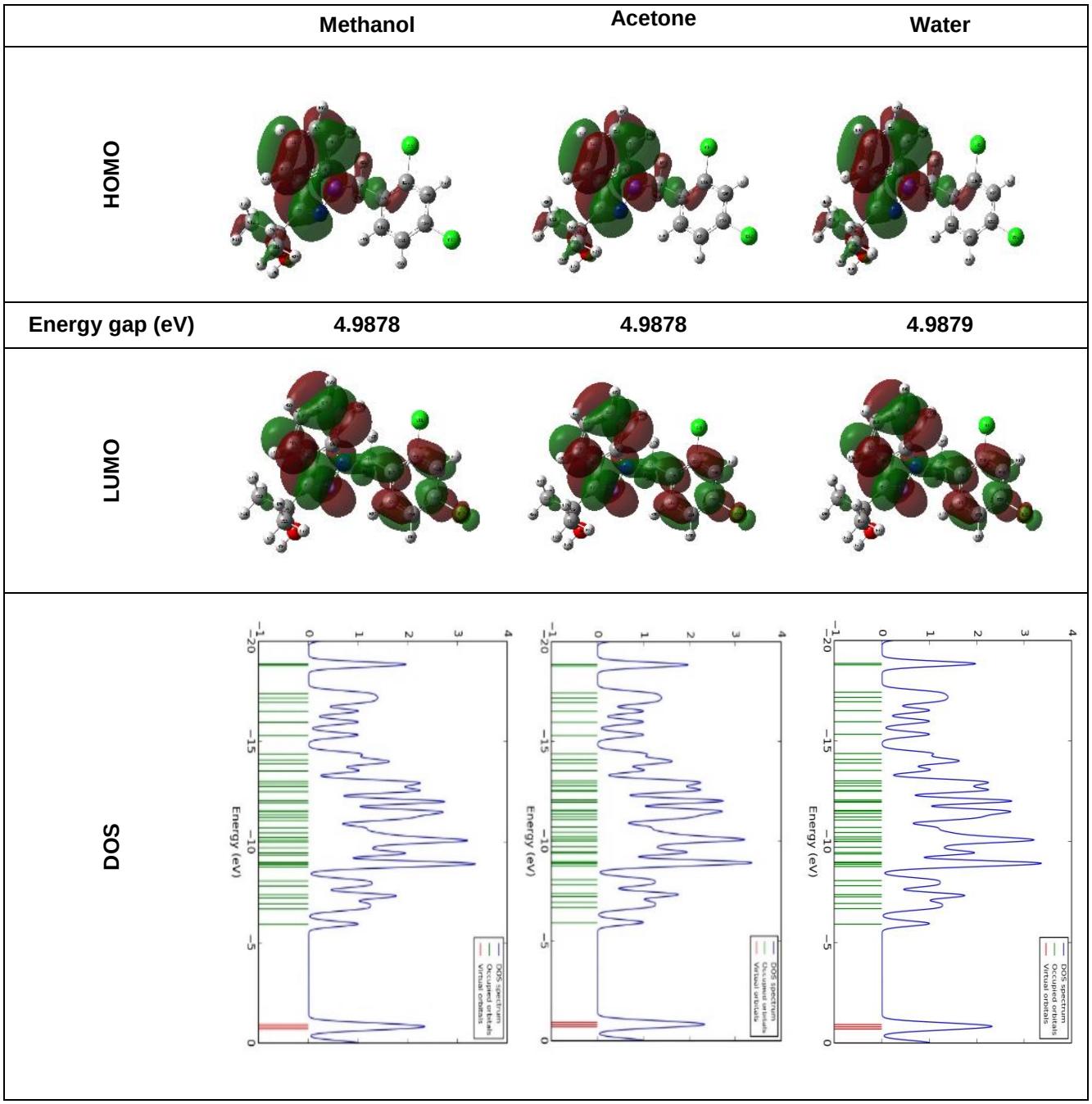

Figure 5. FMO plots and DOS spectra of DCBIP in the polar solvents

3.5 Natural Bonding Orbital (NBO) prediction

NBO analysis examined the stabilizing and destabilizing interactions within molecule by evaluating the interactions between filled and unoccupied orbitals [65]. As shown in Table 6, the lone pair (LP) of nitrogen (N_4) donating to the antibonding orbital (σ*) of the C_8-C_9 bond in the indazole ring provides the strongest stabilization, with a stabilization energy of 40.25 kJ/mol, suggesting that the nitrogen lone pair plays a crucial role in reinforcing the molecule's electronic stability. The second most significant stabilization interaction is the LP(1) → σ*(N_5-C_7) transition, contributing 29.34 kJ/mol, which further enhances the indazole ring's stability by strengthening electron delocalization within the molecule. Additionally, π-π* interactions play a crucial role in stabilizing DCBIP, particularly in C_8-C_9 → N_5-C_7 (27.71 kJ/mol), C_{15}-C_{10} → C_{20}-C_{22} (20.32 kJ/mol), and C_{19}-C_{21}→C_{20}-C_{22} (21.01 kJ/mol). These interactions facilitate effective π-electron delocalization across the conjugated system, further stabilizing the electronic structure. Apart from these major stabilizing effects, LP → σ* transitions from chlorine atoms (Cl_1 and Cl_2) to C_{15}-C_{18} and C_{20}-C_{22} were also observed, though with relatively lower stabilization energies (11.74–12.42 kJ/mol).

Table 6. Selected NBO values of DCBIP

Donor (i)	Type	Acceptor (j)	Type	Type of transition	E(2)[a] (kJ/mol)	E(j)-E(i)[b] (a.u)	F(i,j)[c] (a.u)
C_{15}-C_{10}	π	C_{20}-C_{22}	π*	π - π*	20.32	0.28	0.069
C_8-C_9	π	N_5-C_7	π*	π - π*	27.71	0.26	0.078
C_8-C_9	π	C_{13}-C_{16}	π*	π - π*	19.68	0.028	0.068
C_{19}-C_{21}	π	C_{20}-C_{22}	π*	π - π*	21.01	0.27	0.069
N_4	LP(1)	C_8-C_9	σ*	LP(1)- σ*	40.25	0.29	0.098
N_4	LP(1)	N_5-C_7	σ*	LP(1)- σ*	29.34	0.28	0.082
Cl_2	LP(1)	C_{20}-C_{22}	σ*	LP(1)- σ*	12.42	0.33	0.062
Cl_1	LP(1)	C_{15}-C_{18}	σ*	LP(1)- σ*	11.74	0.34	0.061

[a]E(2) – Mean energy of hyper-conjugative interactions (stabilization energy).

[b]E(j)-E(i) – Energy difference between donor (i) and acceptor (j) natural bonding orbitals.

[c]F(i,j) – Fock matrix element between i and j natural bonding orbital

3.6. Mulliken charge distribution

Mulliken atomic charge analysis provides insight into the electron distribution within molecule [66], revealing charge polarization and electronic behavior at the atomic level as shown in Table S1 (Supplementary Material), the most electronegative atom is oxygen (O_3), with a charge of -0.54232, indicating its strong electron-withdrawing nature due to the hydroxyl (-OH) group. This suggests a potential site for hydrogen bonding and interaction with electrophilic species. The nitrogen atoms N_4 (-0.40505) and N_5 (-0.34159) exhibit significant negative charges, signifying their ability to participate in electron delocalization within the pyrazole ring. C_9 (0.367637) carries the highest positive charge, emphasizing its role in electronic distribution, particularly in stabilizing interactions within the fused pyrazole-benzene system. The dichlorobenzyl ring carbons, C_{18} and C_{22}, show negative charges, with C_{18} (-0.14893) being more negative than C_{22} (-0.09334), indicating slight electronic asymmetry due to the attachment of Cl_1 (-0.01328) and Cl_2 (-0.00929). The chlorine atoms have relatively low negative charges, suggesting limited electron-withdrawing effects compared to other electronegative atoms in the molecule. Carbons C_6 (0.227317) and C_7 (0.270334), which are part of the propan-2-ol and pyrazole rings, exhibit positive charges, reinforcing their role in stabilizing interactions and facilitating electron delocalization. The hydrogen atoms (H_{23}–H_{38}) carry positive charges, with H_{34} (0.298967), attached to O_3, being the most positively charged. These results are visualized in Figure. 6 for better clarity and deeper understanding.

3.7. Molecular Electrostatic Potential (MEP) surface

MEP serves as a valuable tool for identifying electrophilic and nucleophilic reactive regions using surface-colored maps in quantum chemical calculations [67]. The MEP surface map of DCBIP in polar and non-polar solvents, along with electrostatic potential ranges, is presented in Figures. S2 and S3 (Supplementary material). The electrostatic potential range for DCBIP varies between negative and positive values as follows: -7.844×10^{-2} to 7.844×10^{-2} e.s.u. (acetone), -7.540×10^{-2} to 7.540×10^{-2} e.s.u. (chloroform), -7.207×10^{-2} to 7.207×10^{-2} e.s.u. (cyclohexane), -7.885×10^{-2} to 7.885×10^{-2} e.s.u. (methanol), -7.279×10^{-2} to 7.279×10^{-2} e.s.u. (toluene), and -7.929×10^{-2} to 7.929×10^{-2} e.s.u. (water). The molecular structure of DCBIP is influenced by solvent polarity, the electrostatic potential range in polar solvents (acetone, methanol, and water) is higher than in non-polar solvents (toluene, chloroform, and cyclohexane). In the MEP map of DCBIP, red regions over the electronegative oxygen confirm nucleophilic reactive sites, while blue regions over hydrogen atoms at the periphery of aromatic structures indicate electron-deficient areas, marking them as preferred sites for electrophilic attack.

3.8. Thermodynamic properties

From Table 7, the self-consistent field (SCF) energy of -1762.57 Hartree indicates molecular stability, with lower energy reflecting greater stability. The total thermal energy is 198.48 kcal/mol, while the vibrational energy and zero-point vibrational energy (ZPVE) are 197.01 kcal/mol and 186.22 kcal/mol, respectively.

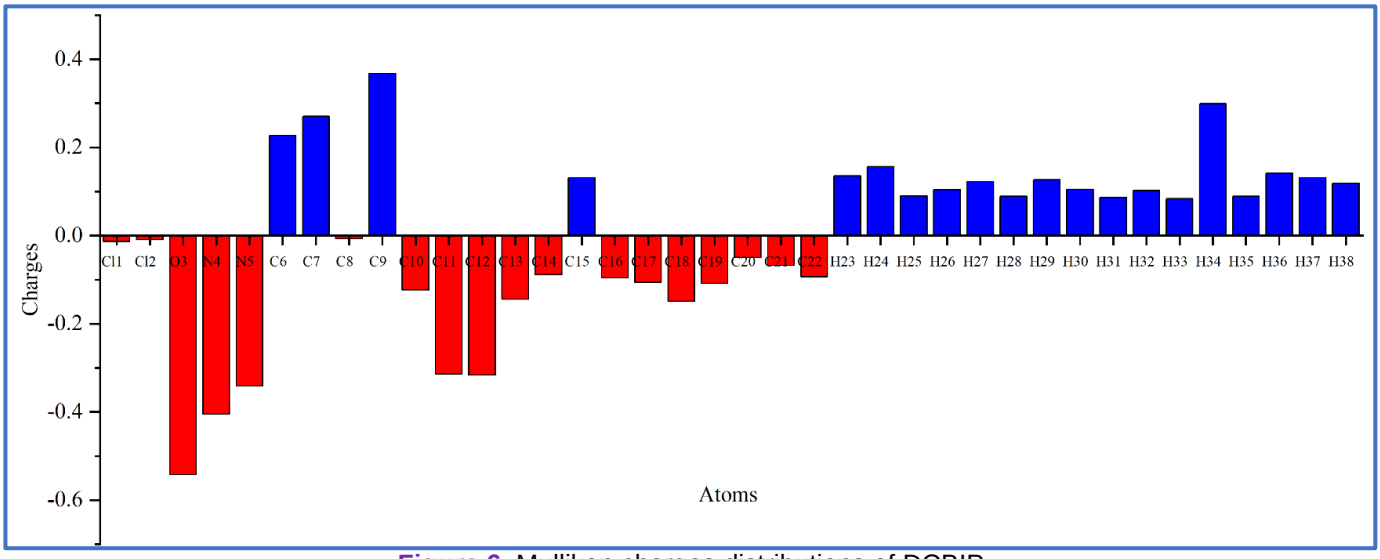

Figure 6. Mulliken charges distributions of DCBIP

Table 7. Calculated thermodynamical parameters of DCBIP

Parameters	**Values**
SCF energy (Hartree)	-1762.57
Total thermal energy (kcal mol^{-1})	198.48
Vibrational energy (kcal mol^{-1})	197.01
Zero-point vibrational energy (kcal mol^{-1})	186.222
Specific heat capacity C_v (cal $mol^{-1}K^{-1}$)	77.31
Entropy, S (cal $mol^{-1}K^{-1}$)	151.197
Dipole moment μ (Debye)	
μ_x	-2.3621
μ_y	0.0705
μ_z	0.7082
μ_{total}	2.4670
Rotational constants (GHz)	
X	0.36285
Y	0.13627
Z	0.11601

The specific heat capacity (77.31 cal $mol^{-1}K^{-1}$) of DCBIP reflects its moderate thermal energy absorption, influenced by vibrational contributions from its complex structure. The dipole moment (μ) of DCBIP is 2.4670 Debye, indicating moderate charge separation. The individual components (μx = -2.3621, μy = 0.0705, μz = 0.7082) suggest that the dipole is predominantly oriented along the x-axis, with smaller contributions from the y- and z-axes. This polarity arises from the electron-withdrawing dichlorobenzyl and hydroxyl groups, which create charge separation in the molecule. The rotational constants of DCBIP reveal its molecular shape and mass distribution, with their significant differences indicating an asymmetric top molecule with distinct moments of inertia along the three principal axes.

3.9. Topological aspects

3.9.1. ELF and LOL

In computational chemistry, understanding electron distribution and bonding characteristics is essential for exploring molecular interactions and chemical reactivity in complex structures.

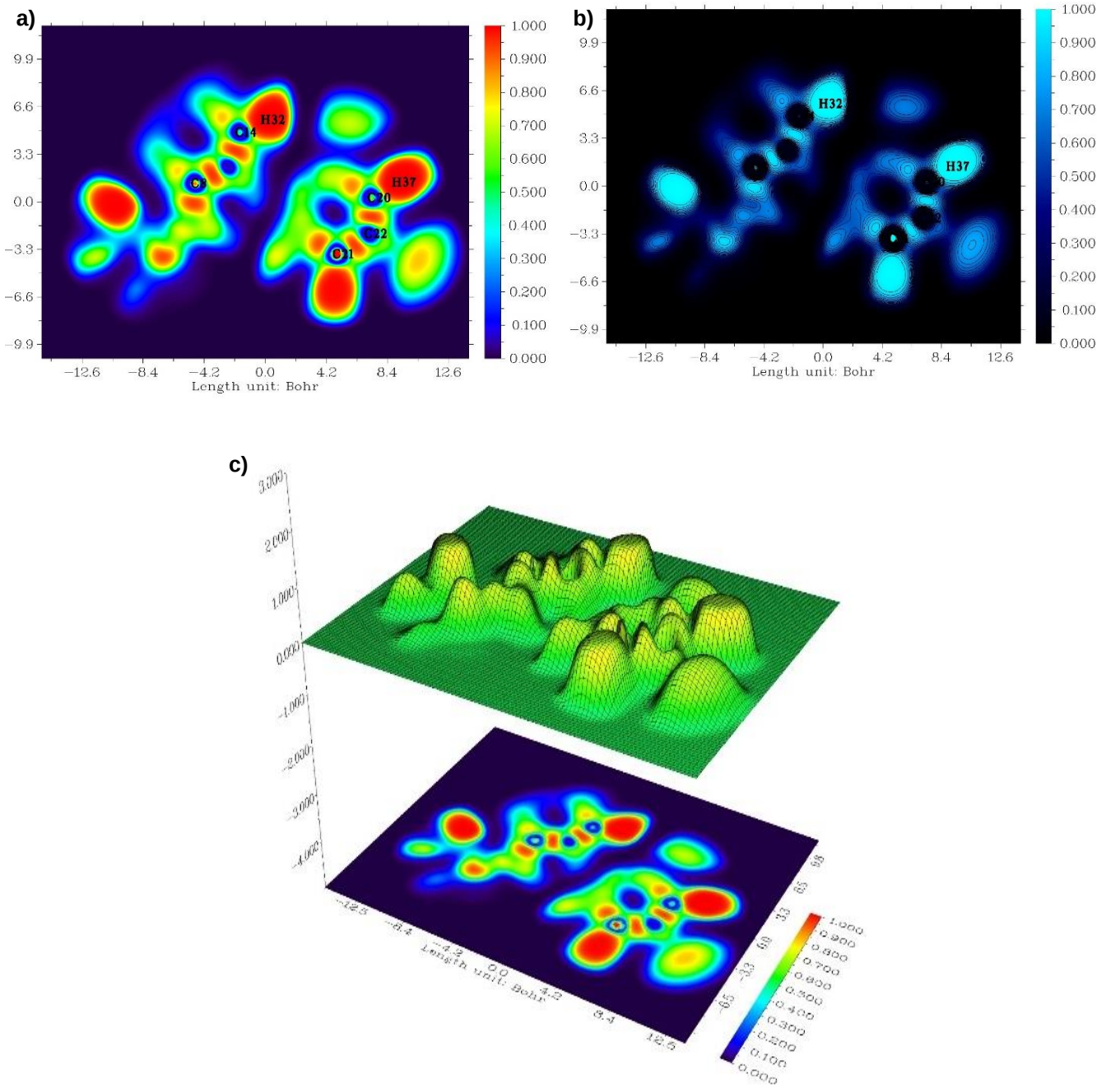

Figure 7(a). ELF diagram with numbering, **(b)** contour map, and **(c)** ELF diagram with projection scheme of DCBIP

Topological approaches, such as the Electron Localization Function (ELF) and Localized Orbital Locator (LOL), provide unique insights into electron localization and bonding characteristics within crystal structures.

The contour maps, color-coded visualizations, and projections of ELF and LOL for DCBIP are presented in Figures. 7 and 8, respectively. The simulated ELF map reveals red regions over the hydrogen atoms H_{32} in the indazole moiety and H_{37} in the dichlorobenzyl moiety, positioned between two chlorine atoms (Cl_1 and Cl_2). This indicates increased electron localization, suggesting the presence of lone pair electron density in these regions. Additionally, the carbon atoms (C_8, C_{14}, C_{20}, C_{21}, and C_{22}) in six-membered rings, enclosed with blue regions, mark the transition from localized to delocalized electronic domains. Similarly, The LOL map further distinguishes these regions, with red regions around the hydrogen atoms (H_{32} and H_{37}) indicating electron localization, while blue regions around the carbon atoms (C_8, C_{14}, C_{20}, C_{21}, and C_{22}) in six-membered rings represent delocalized electronic domains within the crystal structure of DCBIP.

3.9.2 RDG and NCI

Molecular interactions within the crystal structure were investigated using Reduced Density Gradient (RDG) and Non-Covalent Interaction (NCI) analyses to elucidate the nature and strength of non-covalent interactions [68].

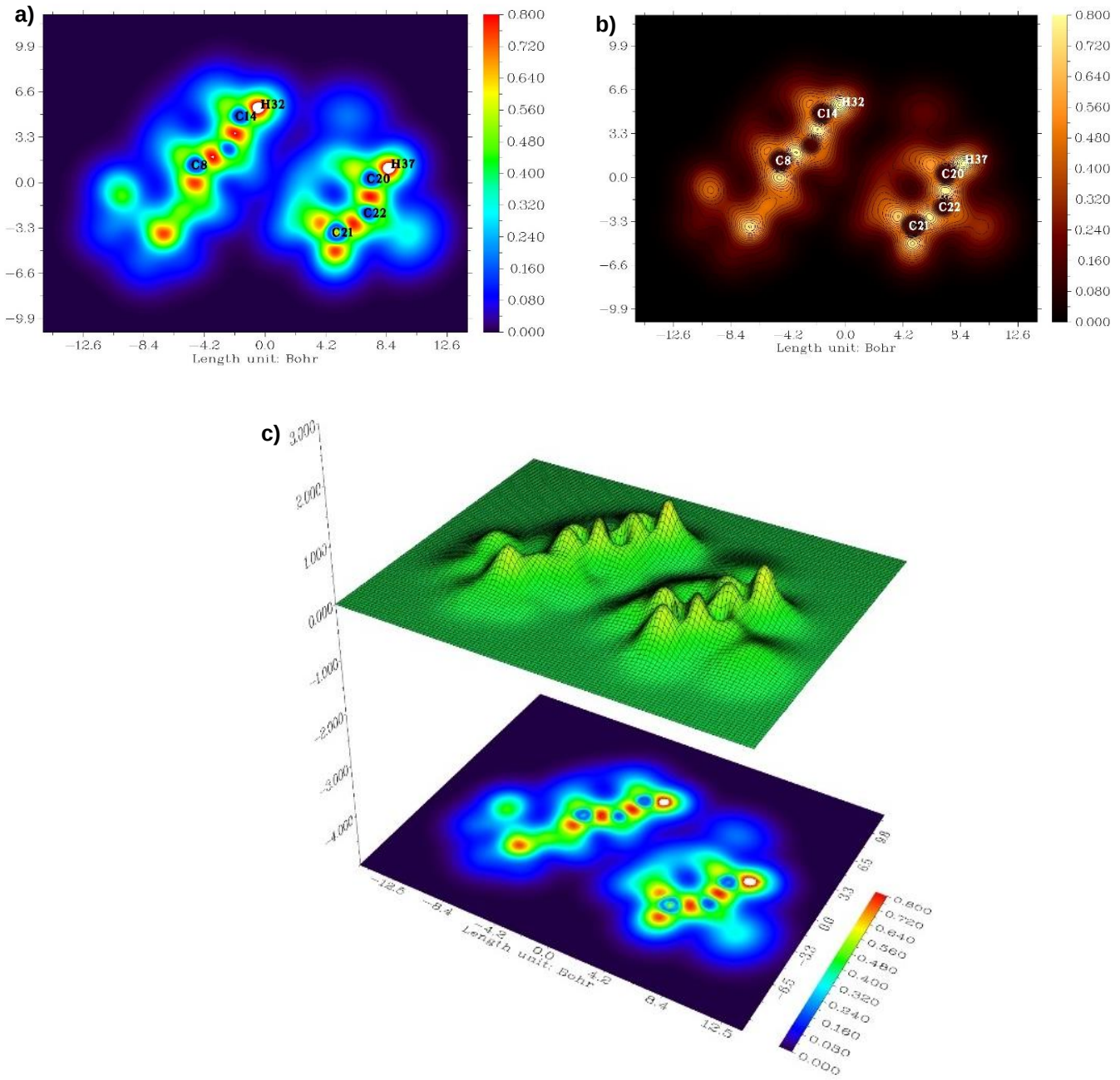

Figure 8.(a) LOL diagram with numbering, **(b)** contour map, and **(c)** LOL diagram with projection scheme of DCBIP

The RDG scatter plot and NCI map for DCBIP, as shown in Figure. 9, display red, blue, and green spikes, which indicate steric repulsion, hydrogen bonding, and van der Waals interactions, respectively. Notably, the presence of prominent green and red spikes in the RDG scatter plot highlights the van der Waals interactions and steric repulsions, which contribute to the overall non-covalent interactions in DCBIP. Furthermore, the NCI iso-surface map reveals red regions embedded within the dichlorobenzyl and indazole rings, while a green region appears between the propan-2-ol side chain and the outer region side of the indazole ring.

3.10. Drug-likeness

In recent decades, simulation tools have become crucial in predicting Absorption, Distribution, Metabolism, and Excretion (ADME) properties, which are vital for developing new drugs [69]. The ADME properties of DCBIP were predicted using computational tools and compared against standard drug-like criteria. The molecular weight (335.23 g/mol) falls well within the acceptable range for oral bioavailability. With two hydrogen bond donors, two hydrogen bond acceptors, and a Log P value of 4.51, DCBIP aligns with Lipinski's Rule of Five, suggesting favorable absorption and permeability.

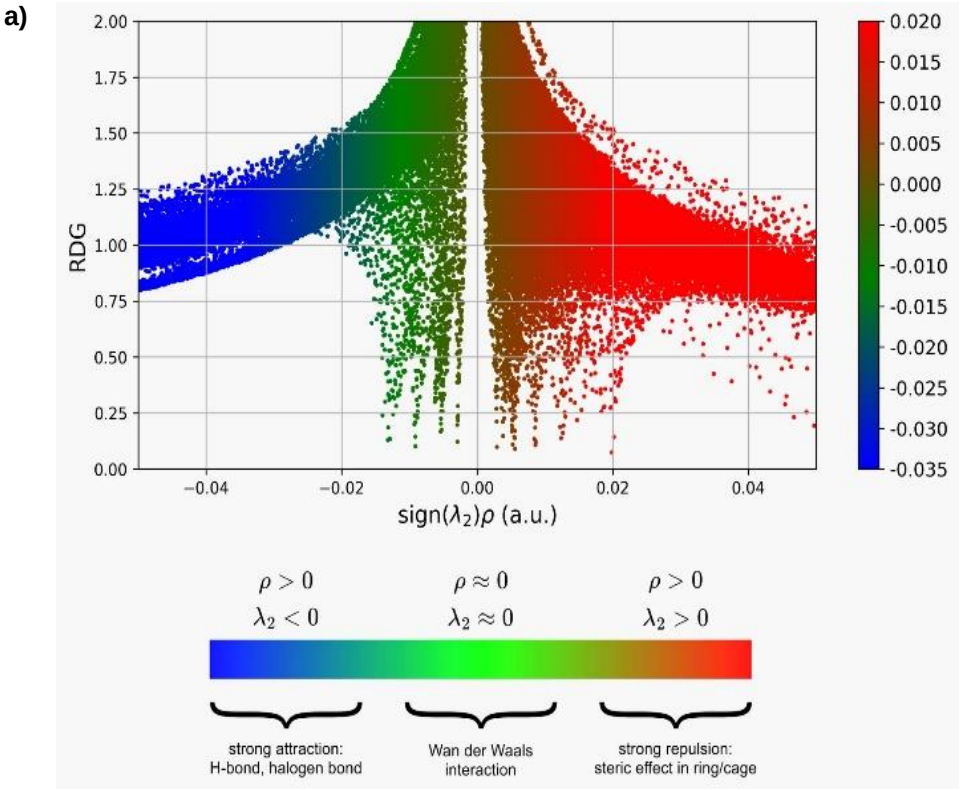

Figure 9. RDG scattered graph (*left*) and NCI iso-surface diagram (*right*) of DCBIP.

Compared to highly polar drugs, its topological polar surface area (TPSA) of 38.05 Å² indicates moderate polarity, balancing solubility and membrane permeability. The compound's bioavailability score of 0.55 is consistent with orally active drugs, reinforcing its drug-like potential. Furthermore, DCBIP exhibits high gastrointestinal (GI) absorption and significant blood-brain barrier (BBB) permeability, suggests potential for central nervous system (CNS) activity. The boiled egg diagram (Fig. 10) provides a visual representation of its absorption and penetration capabilities, while Table S2 (Supplementary material) summarizes the predicted physicochemical parameters.

3.11. Anticonvulsant activity

Molecular docking is a fundamental method in drug discovery and computational research, enabling the prediction macromolecules and ligands affinities. It facilitates the efficient screening and optimization of potential drug candidates [70, 71]. In this study, the structures of the target proteins 1EOU and 5FDC were retrieved from the RCSB Protein Data Bank with resolutions of 2.10 Å and 1.50 Å, respectively. Using the PyMOL program, water molecules and bound ligands were removed to prepare the target proteins for docking, and the refined structures were saved in PDB format. The molecular structure of DCBIP was retrieved from PubChem and optimized before being converted to PDB format for docking.

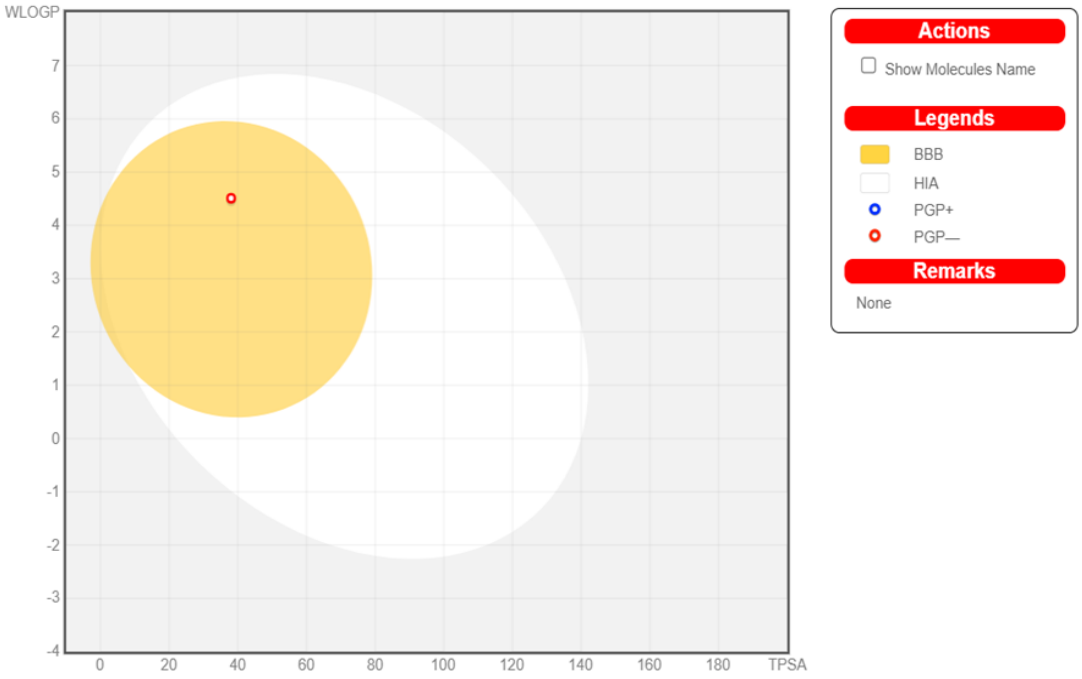

Figure 10. Boiled egg model of DCBIP

Table 8. Molecular docking studies of DCBIP against 1EOU and 5DFC proteins

Proteins	Binding energy (kcal/ mol)	No. of hydrogen bonding	Amino acids	Bond length (Å)	Hydrophobic interaction
1EOU	-6.89	4	Leucine188 Aspargine189 Serine187	2.74 3.14 2.69	Leucine 47 Leucine 44 Lysine 45 Proline 46 Serine 258 Tyrosine 376
5DFC	-7.45	2	Glutamic acid 205 Proline 202	3.33 2.73	Valine 135 Leucine 204 Isoleucine 22 Phenylalanine28 Proline21

AutoDock tool was employed to assess the binding interactions between DCBIP and the target proteins, generating nine possible conformers. The conformer with the lowest docking energy was selected as the most favorable binding mode.

The ligand and protein interaction plots were presented in Figs. 11 and 12, while Table 8 summarizes the key docking parameters. Docking results revealed binding affinities of -6.89 kcal/mol (1EOU) and -7.45 kcal/mol (5FDC), with four and two hydrogen bonds, respectively. These findings highlight the strong interaction potential of DCBIP, suggesting its suitability as a potential anticonvulsant agent.

4. Conclusion

Computational methods were employed to explore the structural, spectroscopic, electronic, and biological properties of the DCBIP. Vibrational, electronic, and chemical shifts analyses identified key spectral features.

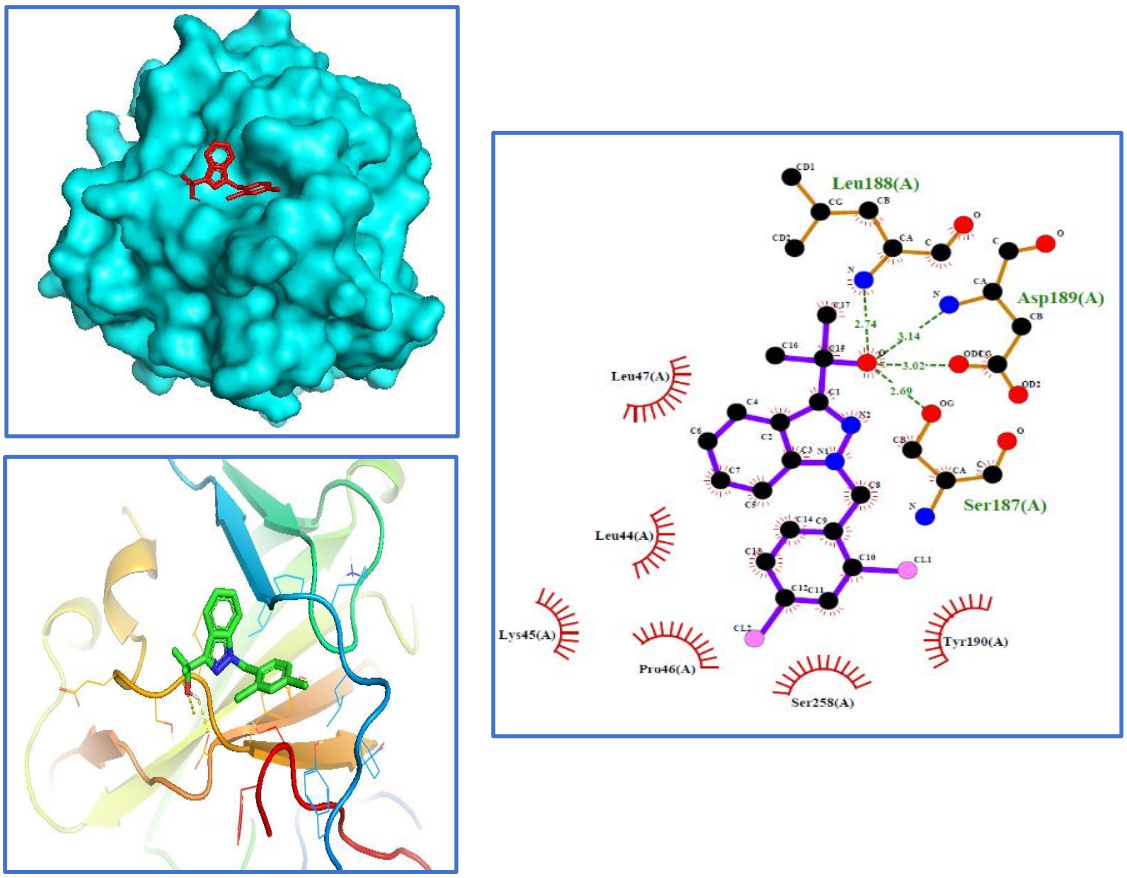

Figure 11. The 3D PyMol and 2D LigPlot⁺ view of DCBIP against 1EOU

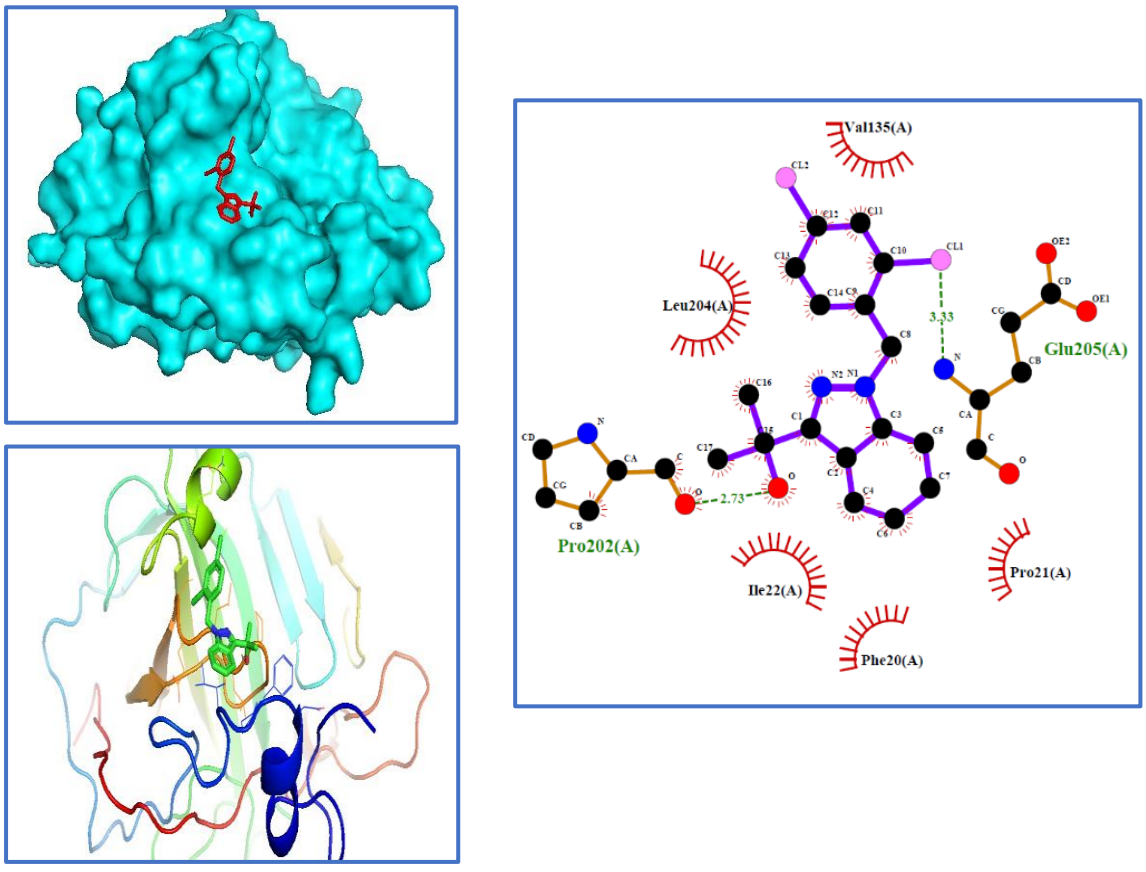

Figure 12. The 3D PyMol and 2D LigPlot⁺ view of DCBIP against 5FDC

In polar solvents, the strongest absorption bands (281.10–281.27 nm) exhibit high oscillator strengths (0.1024–0.1041), indicating strong transition probability. In non-polar solvents, a red shift (281.93–282.63 nm) occurs due to reduced solute-solvent interactions, stabilizing the excited state, while slightly lower oscillator strengths (0.0847–0.0993) suggest a weaker transition probability. The FMO energy gap of DCBIP varies slightly across solvents, indicating minimal solvent influence, with the highest stability in water (4.9879 eV) and methanol (4.9878 eV) and lowest in cyclohexane (4.9797 eV). Electrophilic and nucleophilic sites in DCBIP are identified through Mulliken charge analysis and MEP mapping, while NBO analysis provides insights into electron delocalization and bonding interactions. ELF and LOL highlight bonding in DCBIP, while RDG and NCI map non-covalent interactions essential for stability. A dipole moment of 2.4670 Debye, primarily along the x-axis (μx = -2.3621), characterizes DCBIP, with dichlorobenzyl and hydroxyl groups contributing to its polarity and reactivity. ADME analysis confirms the drug-likeness of DCBIP, while molecular docking demonstrates its strong anticonvulsant potential with binding affinities of -6.89 kcal/mol for 1EOU and -7.45 kcal/mol for 5FDC. These findings provide valuable insights into its therapeutic potential, further supporting *in-vitro* and *in-vivo* studies for the development of novel anticonvulsant drugs.

References

[1] I. Denya, S.F. Malan, J. Joubert, Indazole derivatives and their therapeutic applications: a patent review (2013-2017). Expert opinion on therapeutic patents, 28(6), (2018) 441-453. https://doi.org/10.1080/13543776.2018.1472240

[2] S. Mal, U. Malik, M. Mahapatra, A. Mishra, D. Pal, S.K. Paidesetty, A review on synthetic strategy, molecular pharmacology of indazole derivatives, and their future perspective. Drug Development Research, 83(7), (2022)1469-1504. https://doi.org/10.1002/ddr.21979

[3] W. Song, L. Li, L. Ma, Z. Yang, Z. Zheng, Z. Zhou, Synthesis, crystal structure, DFT, vibrational properties, Hirshfeld surface and antitumor activity studies of a new compound 2-(2-chloro-6-(m-tolyl) imidazo [1, 2-a] pyridin-3-yl)-N, N-diethylacetamide. Journal of Molecular Structure, 1307, (2024) 138052. https://doi.org/10.1016/j.molstruc.2024.138052

[4] A. Singh, D. Malhotra, K. Singh, R. Chadha, P.M.S. Bedi, Thiazole derivatives in medicinal chemistry: Recent advancements in synthetic strategies, structure activity relationship and pharmacological outcomes. Journal of Molecular Structure, 1266, (2022) 133479. https://doi.org/10.1016/j.molstruc.2022.133479

[5] J.F. Lu, P. Huang, D. Zhang, Q. Wang, N. Zheng, R. Wu, Q. Liu, L.X. Jin, X.H. Yu, X.H. Ji, Y.H. Gao,1-(3-Amino-4-morpholino-1H-indazole-1-carbonyl)-N-phenylcyclopropane-1 carboxamide: Design, synthesis, crystal structure, antitumor activity, DFT and Hirshfeld surface analysis. Journal of Molecular Structure, 1210, (2020) 127996. https://doi.org/10.1016/j.molstruc.2020.127996

[6] S. Puri, S. Sawant, K. Juvale, A comprehensive review on the indazole based derivatives as targeted anticancer agents. Journal of Molecular Structure, 1284 (2023) 135327. https://doi.org/10.1016/j.molstruc.2023.135327

[7] A. Tanitame, Y. Oyamada, K. Ofuji, Y. Kyoya, K. Suzuki, H. Ito, M. Kawasaki, K. Nagai, M. Wachi, J.I. Yamagishi, Design, synthesis and structure–activity relationship studies of novel indazole analogues as DNA gyrase inhibitors with Gram-positive antibacterial activity. Bioorganic & medicinal chemistry letters, 14(11), (2024) 2857-2862. https://doi.org/10.1016/j.bmcl.2004.03.044

[8] M. Minu, A. Thangadurai, S.R. Wakode, S.S. Agrawal, B. Narasimhan, Synthesis, antimicrobial activity and QSAR studies of new 2, 3-disubstituted-3, 3a, 4, 5, 6, 7-hexahydro-2H-indazoles. Bioorganic & medicinal chemistry letters, 19(11), (2009) 2960-2964. https://doi.org/10.1016/j.bmcl.2009.04.052

[9] R.P. Chaudhary, P. Gautam, D. Gautam, I. Mittal, Ultrasound assisted regioselective synthesis, photophysical and structural studies of 1-substituted indazol-4 (5H)-ones and enaminodiketones of dimedone. Journal of Molecular Structure, 1228, (2021) 129710. https://doi.org/10.1016/j.molstruc.2020.129710

[10] E.A. Abdelsalam, W.A. Zaghary, K.M. Amin, N.A. Abou Taleb, A.A. Mekawey, W.M. Eldehna, H.A. Abdel-Aziz, S.F. Hammad, Synthesis and in vitro anticancer evaluation of some fused indazoles, quinazolines and quinolines as potential EGFR inhibitors. Bioorganic Chemistry, 89, (2019) 102985. https://doi.org/10.1016/j.bioorg.2019.102985

[11] P.J. Park JoonSeok, Y.K. Yu KyungA, K.T. Kang TaeHee, K.S. Kim SungHoon, S.Y. Suh, Y. Ger, Discovery of novel indazole-linked triazoles as antifungal agents. Bioorganic & Medicinal Chemistry Letters, 17, (2007) 3486-3490. https://doi.org/10.1016/j.bmcl.2007.03.074

[12] K.P. Harish, K.N. Mohana, L. Mallesha, Synthesis of indazole substituted-1, 3, 4-thiadiazoles and their anticonvulsant activity. Drug invention today, 5(2), (2013) 92-99. https://doi.org/10.1016/j.dit.2013.06.002

[13] A. Upadhyay, S.K. Srivastava, S.D. Srivastava, Conventional and microwave assisted synthesis of Some new N-[(4-oxo-2-substituted aryl −1, 3-thiazolidine)-acetamidyl]-5-nitroindazoles and its antimicrobial activity. European Journal Medicinal Chemistry, 45(9), (2010) 3541-3548.

https://doi.org/10.1016/j.ejmech.2010.04.029

[14] F.A.B. Schutz, T.K. Choueiri, C.N. Sternberg, Pazopanib: clinical development of a potent anti-angiogenic drug. Critical Reviews in Oncology/Hematology, 77(3), (2011) 163-171. https://doi.org/10.1016/j.critrevonc.2010.02.012

[15] R. Tandon, I. Singh, V. Luxami, N. Tandon, K. Paul, Recent Advances and Developments of in vitro Evaluation of Heterocyclic Moieties on Cancer Cell Lines. The Chemical Record, 19(2-3), (2019) 362-393. https://doi.org/10.1002/tcr.201800024

[16] M. Bersanelli, M. Brunelli, L. Gnetti, U. Maestroni, S. Buti, Pazopanib as a possible option for the treatment of metastatic non-clear cell renal carcinoma patients: a systematic review. Therapeutic Advances in Medical Oncology, 12, (2020) 1758835920915303. https://doi.org/10.1177/1758835920915303

[17] G. Sonpavde, T.E. Hutson, B.I. Rini, Axitinib for renal cell carcinoma. Expert opinion on investigational drugs, 17(5), (2008) 741-748. https://doi.org/10.1517/13543784.17.5.741

[18] G. Sonpavde, T.E. Hutson, C.N. Sternberg, Pazopanib, a potent orally administered small-molecule multitargeted tyrosine kinase inhibitor for renal cell carcinoma. Expert opinion on investigational drugs, 17(2), (2008) 253-261. https://doi.org/10.1517/13543784.17.2.253

[19] M. Rouhani, Evaluation of structural properties and antioxidant capacity of Proxison: A DFT investigation. Computational and Theoretical Chemistry, 1195, (2021) 113096. https://doi.org/10.1016/j.comptc.2020.113096

[20] K. Anandan, P. Kolandaivel, R. Kumaresan, Ab initio and DFT studies on tautomerism of indazole in gaseous and aqueous phases. Journal of Molecular Structure: Theochem, 686(1-3), (2004) 83-89. https://doi.org/10.1016/j.theochem.2004.08.014

[21] B. Morzyk-Ociepa, K. Szmigiel-Bakalarz, M. Nentwig, O. Oeckler, M. Malik, Structural (X-ray), spectroscopic (FT-IR, FT-Raman) and computational (DFT) analysis of intermolecular interactions in 1H-indazole-3-carbaldehyde. Journal of Molecular Structure, 1237, (2021) 130318. https://doi.org/10.1016/j.molstruc.2021.130318

[22] P.V. Ramana, Y.R. Krishna, K.C. Mouli, Experimental FT-IR and UV–Vis spectroscopic studies and molecular docking analysis of anti-cancer drugs Exemestane and Pazopanib. Journal of Molecular Structure, 1263, (2022) 133051. https://doi.org/10.1016/j.molstruc.2022.133051

[23] M.M. Andres-Mach, M. Dudra-Jastrzebska, M. Mohamed, K.M. Sawicka, J. Kozinska, S.J. Czuczwar, 7-Nitroindazole enhances dose-dependently the anticonvulsant activities of conventional antiepileptic drugs in the mouse maximal electroshock-induced seizure model. Pharmacological reports, 58(660), (2006) 660-671.

[24] N. Matsumura, K. Kikuchi-Utsumi, K. Sakamaki, M. Watabe, K. Aoyama, T. Nakaki, Anticonvulsant action of indazole. Epilepsy research, 104(3), (2013) 203-216. https://doi.org/10.1016/j.eplepsyres.2012.11.001

[25] Parr, R. G. (1989). Density functional theory of atoms and molecules. In Horizons of Quantum Chemistry: Proceedings of the Third International Congress of Quantum Chemistry, Springer, Netherlands.

[26] W. Kohn, L.J. Sham, Self-consistent equations including exchange and correlation effects. Physical review, 140, (1965) A1133. https://doi.org/10.1103/PhysRev.140.A1133

[27] P. Hohenberg, W. Kohn, Inhomogeneous electron gas. Physical review, 136, (1964) B864. https://doi.org/10.1103/PhysRev.136.B864

[28] D.R. Salahub, M.C. Zerner, The Challenge of d and f Electrons: Theory and Computation. American Chemical Society, 394, (1989). https://doi.org/10.1021/bk-1989-0394

[29] A.D. Becke, Density-functional thermochemistry. I. The effect of the exchange-only gradient correction. The Journal of chemical physics, 96(3), (1992) 2155-2160. https://doi.org/10.1063/1.462066

[30] C. Lee, W. Yang, R.GParr, Development of the Colle-Salvetti correlation-energy formula into a functional of the electron density. Physical review B, 37(2), (1988) 785. https://doi.org/10.1103/PhysRevB.37.785

[31] B. Miehlich, A. Savin, H. Stoll, H. Preuss. Results obtained with the correlation energy density functionals of Becke and Lee, Yang and Parr. Chemical Physics Letters, 157(3), (1989) 200-206. https://doi.org/10.1016/0009-2614(89)87234-3

[32] M. J. Frisch, (2009). Gaussion 09W, Revision A. 02, Gaussion Inc. Walling ford, CT.

[33] M. Petersilka, U.J. Gossmann, E.K.U. Gross. Excitation energies from time-dependent density-functional theory. Physical review letters. 76(8), (1996) 1212. https://doi.org/10.1103/PhysRevLett.76.1212

[34] E. Runge, E.K.U Gross. Density-functional theory for time-dependent systems. Physical review letters, 52(12), (1984) 997. https://doi.org/10.1103/PhysRevLett.52.997

[35] R. Bauernschmitt, R. Ahlrichs. Treatment of electronic excitations within the adiabatic approximation of time dependent density functional theory. Chemical Physics Letters,

256(4-5), (1996) 454-464. https://doi.org/10.1016/0009-2614(96)00440-X

[36] R. Ditchfield, Self-consistent perturbation theory of diamagnetism: I. A gauge-invariant LCAO method for NMR chemical shifts. Molecular Physics, 27(4), (1974) 789-807. https://doi.org/10.1080/00268977400100711

[37] K. Wolinski, J. F. Hinton, P. Pulay, Efficient implementation of the gauge-independent atomic orbital method for NMR chemical shift calculations. Journal of the American Chemical Society, 112(23), (1990) 8251-8260. https://doi.org/10.1021/ja00179a005

[38] J.R. Cheeseman, G.W. Trucks, T.A. Keith, M.J. Frisch, A comparison of models for calculating nuclear magnetic resonance shielding tensors. The Journal of chemical physics, 104(14), (1996) 5497-5509. https://doi.org/10.1063/1.471789

[39] J. Gauss, Calculation of NMR chemical shifts at second-order many-body perturbation theory using gauge-including atomic orbitals. Chemical physics letters, 191(6), (1992) 614-620. https://doi.org/10.1016/0009-2614(92)85598-5

[40] J.A. Bohmann, F. Weinhold, T.C. Farrar, Natural chemical shielding analysis of nuclear magnetic resonance shielding tensors from gauge-including atomic orbital calculations. The Journal of chemical physics, 107(4), (1997) 1173-1184. https://doi.org/10.1063/1.474464

[41] R.D.I.I. Dennington, T.A. Keith, J.M. Millam, (2016). GaussView, version 6.0. 16. Semichem Inc Shawnee Mission KS, 13(1).

[42] G.A. Zhurko, D.A. Zhurko, (2009). Chemcraft Program Version 1.6 (Build 315).

[43] A. Daina, O. Michielin, V. Zoete, SwissADME: a free web tool to evaluate pharmacokinetics, drug-likeness and medicinal chemistry friendliness of small molecules. Journal of Scientific Reports, 7(1), (2017) 42717. https://doi.org/10.1038/srep42717

[44] G.M. Morris, R. Huey, W. Lindstrom, M.F. Sanner, R.K. Belew, D.S. Goodsell, A.J. Olson, AutoDock4 and AutoDockTools4: Automated docking with selective receptor flexibility. Journal Computational Chemistry, 30, (2009) 2785-2791. https://doi.org/10.1002/jcc.21256

[45] R.A. Laskowski, M. B. Swindells, LigPlot+: multiple ligand–protein interaction diagrams for drug discovery, 51, (2011) 2778-2786. https://doi.org/10.1021/ci200227u

[46] S. Yuan, HCS. Chan, Z. Hu. Using PyMOL as a platform for computational drug design. Wiley Interdisciplinary Reviews: Computational Molecular Science, 7(2), (2017) e1298. https://doi.org/10.1002/wcms.1298

[47] T. Lu, F. Chen, Multiwfn: a multifunctional wavefunction analyzer. Journal of Computational Chemistry, 33(5), (2012) 580-592. https://doi.org/10.1002/jcc.22885

[48] S. Armakovic, S.J. Armakovic, Atomistica. Online–web application for generating input files for ORCA molecular modelling package made with the Anvil platform. Molecular simulation, 49(1), (2023) 117-123. https://doi.org/10.1080/08927022.2022.2126865

[49] S. Armakovic, S.J. Armakovic, Online and desktop graphical user interfaces for xtb programme from atomistica. online platform. Molecular Simulation, 50(7-9), (2024) 560-570. https://doi.org/10.1080/08927022.2024.2329736

[50] L. K. Mapp, S.J. Coles, S. Aitipamula, CCDC 1531957: Experimental Crystal Structure Determination, 2017,

[51] A. Ram Kumar, S. Selvaraj, A.S. Vickram, GP Sheeja Mol, Shikha Awasthi, M. Thirunavukkarasu, M. Selvaraj, S. Basumatary. Exploring the potential of diosgenin as a promising antitumor agent through comprehensive spectroscopic characterization, solvent–solute interactions, topological properties, Hirshfeld surface, and molecular docking interactions with 2NZT and 2I1V proteins. Spectrochimica Acta Part A: Molecular and Biomolecular Spectroscopy, 327, (2025), 125349. https://doi.org/10.1016/j.saa.2024.125349

[52] V. Vijayalakshmi, N. Kanagathara, Janczak Jan, M.K. Marchewka, Mohammad Azam, K. Senthilkumar, Structural, spectroscopic and second harmonic generation evaluation of 1, 2, 4-triazolinium tartrate-tartaric acid as a promising nonlinear optical material. Optical Materials, 147, (2024) 11469. https://doi.org/10.1016/j.optmat.2023.114694

[53] S. Gunasekaran, S. Kumaresan, S. Seshadri, S. Muthu, Vibrational spectra and normal coordinate analysis of structure of procarbazine. Indian Journal of Pure and Applied Physics, (2008). https://doi.org/10.1007/s12043-008-0183-0

[54] P. Divya, V. S. Jeba Reeda, V. Bena Jothy. Fungicide compound 2, 3-dichloronaphthalene-1, 4-dione: Non-covalent interactions (QTAIM, RDG and ELF), combined vibrational spectroscopic investigations using DFT approach with experimental analysis, electronic, molecular docking scrutiny in-vitro assay and thermodynamic property analysis. Journal of Molecular Liquids, 400, (2024) 124544. https://doi.org/10.1016/j.molliq.2024.124544

[55] N. Suma, D. Aruldhas, I. Hubert Joe, S. Balachandran, A. Ronaldo Anuf, Arun Sasi, and Jesby George, Vibrational spectra, hydrogen bonding analysis and herbicidal activity study of mefenacet: A DFT approach. Journal of Molecular Structure, 1201, (2020) 127203. https://doi.org/10.1016/j.molstruc.2019.127203

[56] C. Karnan, A. Ram Kumar, S. Selvaraj, Quantum chemical computational studies on the structural aspects, spectroscopic properties, hirshfeld surfaces, donor-acceptor interactions and molecular docking of clascosterone: a promising antitumor agent. International Research Journal of Multidisciplinary Technovation, 6(4), (2024) 32-53. https://doi.org/10.54392/irjmt2444

[57] M.T. Gulluoglu, Y. Erdogdu, S. Yurdakul, Molecular structure and vibrational spectra of piperidine and 4-methylpiperidine by density functional theory and ab initio Hartree–Fock calculations. Journal of molecular structure, 834, (2007) 540-547. https://doi.org/10.1016/j.molstruc.2007.01.023

[58] R.M. Silverstein, G. Clayton Bassler, Spectrometric identification of organic compounds. Journal of Chemical Education, 39(11), (1962) 546. https://doi.org/10.1021/ed039p546

[59] S. Selvaraj, P. Rajkumar, M. Kesavan, S. Gunasekaran, S. Kumaresan, 2018. Experimental and theoretical investigations on spectroscopic properties of tropicamide. Journal of Molecular Structure, 1173, (2018) 52-62. https://doi.org/10.1016/j.molstruc.2018.06.097

[60] C.Y. Panicker, H.T. Varghese, K.C. Mariamma, K. John, S. Mathew, J. Vinsova, C. Van Alsenoy, Y.S. Mary, Spectroscopic investigations and computational study of 2-[acetyl (4-bromophenyl) carbamoyl]-4-chlorophenyl acetate. Journal of Raman Spectroscopy, 41(6), (2010) 707-716. https://doi.org/10.1002/jrs.2492

[61] J.N. Cheerlin Mishma, V. Bena Jothy, B. Narayana, Suresh N Kodlady, Naiyf S. Alharbi, Ghulam Abbas, S. Muthu, Synthesis, DFT, solvent effect and biological attributes of NLO active 4-bromo-2-((2-(2, 4-Dinitrophenyl) hydrazono) methyl) phenol-Potent drug anti-brain cancer. Journal of Molecular Structure, 1289, (2023) 135839. https://doi.org/10.1016/j.molstruc.2023.135839

[62] S. Selvaraj, A. Ram Kumar, T. Ahilan, M. Kesavan, S. Gunasekaran, S. Kumaresan, Multi spectroscopic and computational investigations on the electronic structure of oxyclozanide. Journal of the Indian Chemical Society, 99(10), (2022) 100676. https://doi.org/10.1016/j.jics.2022.100676

[63] K.R. Cousins (2011). Computer review of ChemDraw ultra 12.0.

[64] M. Karabacak, E. Kose, A. Atac, A. M. Asiri, M. Kurt, Monomeric and dimeric structures analysis and spectroscopic characterization of 3, 5-difluorophenylboronic acid with experimental (FT-IR, FT-Raman, 1H and 13C NMR, UV) techniques and quantum chemical calculations. Journal of molecular structure, 1058, (2014), 79-96. https://doi.org/10.1016/j.molstruc.2013.10.064

[65] M.A.S. Sakr, F.F. Sherbiny, A.A. Sh. El-Etrawy, Hydrazone-based Materials; DFT, TD-DFT, NBO Analysis, Fukui Function, MESP Analysis, and Solar Cell Applications. Journal of Fluorescence, 32, (2022) 1857-1871. https://doi.org/10.1007/s10895-022-03000-6

[66] P. Jayaprakash, S. Selvaraj, A. Ram Kumar. A new organic compound (C9H12N2O2): crystal structure, characterization, Hirshfeld surface analysis, electronic properties, NLO properties, DFT calculation and molecular docking. Solid State Sciences, 154, (2024) 107587. https://doi.org/10.1016/j.solidstatesciences.2024.107587

[67] R. Suja, A. Rathika, V. S. Jeba Reeda, A. Arun Kumar, P. Divya, Synthesis, spectroscopic analysis (FT-IR, FT-Raman, UV, NMR), non-covalent interactions (RDG, IGM) and dynamic simulation on Bis (8 hydroxy quinoline) salicylate salicylic acid. Journal of Molecular Structure, 1310, (2024) 138231. https://doi.org/10.1016/j.molstruc.2024.138231

[68] V.S. Jeba Reeda, P. Divya, A. Amala Jeya Ranchani, A. Manikandan, Shakeel Alvi, Rashid Ali, Nazia Siddiqui, Nazrul Haq, S. Muthu, Ray Butcher, Saleem Javed, Comprehensive analysis of 2, 5-dimethyl-1-(naphthalen-1-yl)-1H-pyrrole: X-ray crystal structure, spectral, computational, molecular properties, docking studies, molecular dynamics, and MMPBSA. Journal of Molecular Structure, 1321, (2025) 140062. https://doi.org/10.1016/j.molstruc.2024.140062

[69] X. Chen, H. Li, L. Tian, Q. Li, J. Luo, Y. Zhang, Analysis of the physicochemical properties of acaricides based on Lipinski's rule of five. Journal of computational biology, 27(9), (2020) 1397-1406. https://doi.org/10.1089/cmb.2019.0323

[70] E. Mohanapriya, S. Elangovan, N. Kanagathara, M.K. Marchewka, Jan Janczak, P. Revathi, Density functional theory calculations, structural and spectroscopic characterization, and solvent-dependent HOMO-LUMO studies of 2-nitro-4-methylanilinium benzenesulfonate, Journal of Molecular Structure, 1317, (2024) 139147. https://doi.org/10.1016/j.molstruc.2024.139147

[71] S. Akshay Kalyan, N. Kanagathara, M.K. Marchewka, Jan Janczak, K. Senthilkumar, Structure, Spectroscopy, and Theoretical insights on Co-crystals of 2, 4-Diamino-6-Methyl-1, 3, 5-Triazine Bis (4-Aminobenzoic acid) Monohydrate as a promising anti-cancer agent, Physica B: Condensed Matter, 679, (2024) 415807. https://doi.org/10.1016/j.physb.2024.415807

Author Contribution statement

J. Jenifer: Writing - Original draft, Methodology, Data Analysis. A. Ram Kumar: Writing - Review & Editing,

Visualization and Validation. S. Selvaraj: Writing - Review & Editing, Conceptualization and Supervision.

Funding

The authors declare that no funds, grants or any other support were received during the preparation of this manuscript.

Competing Interests

The authors declare that there are no conflicts of interest regarding the publication of this manuscript.

Data Availability

The data supporting the findings of this study can be obtained from the corresponding author upon reasonable request.

Has this article screened for similarity?

Yes

About the License